Controlling the Quality of Two-Way Euler/Lagrange Numerical Modeling of Bubbling and Spouted Fluidized Beds Dynamics

Manuel Bernard,[†] Eric Climent,[‡] and Anthony Wachs*[,§,∥]

[†]Fluid Mechanics Department, IFP Energies Nouvelles, 69360 Solaize, France

[‡]Institut de Mécanique des Fluides de Toulouse, Université de Toulouse - CNRS, INPT, UPS - 31400 Toulouse, France

[§]Department of Mathematics, University of British Columbia, 1984 Mathematics Road, Vancouver, BC, Canada V6T 1Z2

[∥]Department of Chemical & Biological Engineering, University of British Columbia, 2360 East Mall, Vancouver, BC, Canada V6T 1Z3

ABSTRACT: We numerically simulate three-dimensional fluidized beds of monodisperse spheres using a two-way Euler/Lagrange method. Particles trajectories are tracked in a Lagrangian way, and particles collisions are computed by a soft sphere model. The fluid conservation equations are written in a classical Eulerian fashion and are locally averaged on cells 1 order of magnitude larger than particles. We detail the equations of the model and their numerical implementation. We study the influence of numerical parameters and simulation domain size on computed results in a biperiodic fluidized bed. We then validate the model against theoretical results for a bubbling fluidized bed and against experimental data for a single- and multi-nozzle spouted bed. Finally, we investigate the influence of the Coulomb friction coefficient magnitude on a single-nozzle spouted bed dynamics in order to emphasize the importance of tangential friction in such processes.

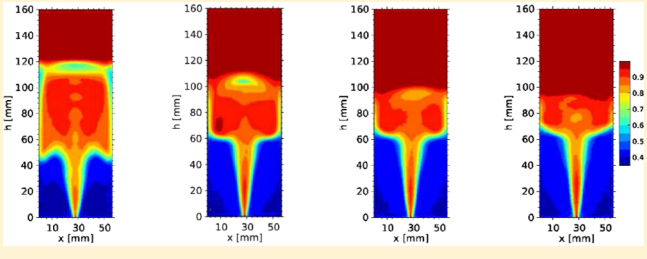

1. INTRODUCTION

Fluid−particle two-phase flows such as fluidized beds are involved in several industrial domains as, e.g., chemical and process engineering. In fact, due to its high heat and mass transfer rates, the fluidized bed flow configuration is widely used in coal gasification, chemical looping combustion (CLC), atmospheric or pressurized fluidized bed combustion (FBC), and fluid catalytic cracking (FCC). Solid particle diameters generally range from a few tens of micrometers to a few millimeters. In fluidized or fixed beds, a lighter fluid, that can be either a liquid or a gas, is injected at the bottom wall of the reactor and flows out at the top wall of the reactor. If the force exerted on particles by the fluid flow is strong enough (and actually stronger than the net weight of particles), particles are fluidized, i.e., they are set in motion. In a reactor containing up to several billions of particles, their spatial distribution is very often heterogeneous. Indeed, particles trajectories are affected both by hydrodynamic interactions with the surrounding fluid flow and collisions with neighboring particles and wall boundaries. This leads to the formation of particles clusters and void areas called fluid bubbles. The typical size of these structures can be significantly larger than the average particle diameter.[1−3] As a result of this intricate dynamics of the fluid−particle system, the whole bed expands until it reaches a pseudosteady state over which its height fluctuates either slightly or markedly depending on the flow regime. This dynamics of fluidized beds is undoubtedly multiscale, from the microscale of the fluid flow around individual particles and interparticle contacts to the mesoscale of particle clusters and fluid bubbles, and eventually to the macro-scale of the whole bed behavior. Related to these three spatial scales, three corresponding modeling strategies are often adopted. At the microscale, Navier−Stokes equations are solved over the fluid domain on a grid much thinner than each individual particle and particles trajectories are fully described. This approach enables one to accurately compute the flow kinematics around each solid particle. The fluid−solid interaction is then reliably computed by any appropriate integration of the fluid stress tensor over the particle surface. The corresponding simulations are high-fidelity provided the fluid cell size over particle diameter ratio is small enough (at least 1/10 and sometimes up to 1/40 to guarantee accurate computed solutions). The aftermath of this constraint on the grid size is the rather limited size of systems that can be reasonably simulated even with massively parallel codes on the most powerful supercomputers. Apart from a few exceptions,[4] microscale simulations are generally limited to a few thousands of particles. At the macroscale, both the fluid and solid phases are described by locally averaged continuous conservation equations. Since the solid phase is assumed to be continuous, particles trajectories are not individually tracked anymore, and instead, the solid phase is described in terms of a local volume fraction or porosity. This kind of approach, often referred to as the Euler−Euler model,

DOI: 10.1021/acs.iecr.6b03627

has been widely applied to fluidized beds by Gidaspow (see the Two Fluid Model (TFM) in, e.g., ref 5) and enables one to examine systems containing billions of particles representative of a human-size chemical process. The mesoscale model represents a compromise between microscale models and macroscale models. In the mesoscale model, often called two-way Euler/Lagrange or DEM-CFD (for DEM (Discrete Element Method)-CFD (Computational Fluid Dynamics)), the fluid phase is locally averaged as in the macroscale model, but particles are still tracked individually as in the microscale model. Particle−particle and particle−wall collisions are precisely handled while fluid−solid interactions rely on closure laws. However, fluid−solid interactions are deemed to be more accurately modeled than in macroscale Euler−Euler approaches. This results in a better prediction of the dynamics of fluid bubbles and particles clusters comprising several thousands of particles or more. Conceptually, fluid cells in the mesoscale model are much smaller than in the macroscale Euler−Euler model but much larger than in the microscale model. Furthermore, several numerical knacks were developed over the past 20 years to improve computing performances in such a way that nowadays simulations with up to a few tens of millions or even a few hundreds of millions of particles are attainable.[6] Typically, a system containing such a number of particles mimics pretty well a small size 3D experimental fluidized bed and hence offers the opportunity to perform a direct simulations−experiments comparison. It is particularly important to emphasize that the dynamics of a fluidized bed is fully three-dimensional and that consequently the attempt to model and understand the global behavior of a bed with 2D simulations is mostly worthless.[6]

The two-way Euler−Lagrange approach has been first introduced by Tsuji et al.[7] in the early 1990s. In the pioneering form of the model, collisions were handled by a soft sphere approach. A couple of years later, Hoomans et al.[8] proposed a DEM-CFD model based on a hard sphere principle. Such a collision approach is better suited to dilute fluid/particles mixture since collisions are assumed to be binary and instantaneous and therefore request to be treated one after another.[9] Then, the formulation of the model was improved by several research groups. In particular, the interested reader will refer to the prolific scientific exchange between the group of Xu and Yu and Hoomans and his collaborators[10−12] on the consistency of the model.

The total hydrodynamic force, i.e., integration of fluid stress tensor over particle surface can be expressed as the sum of different hydrodynamic contributions, mainly drag force, lift force, added mass force, and Basset force. For gas-particles flows, the drag force is the leading contribution, and correspondingly, the other contributions are generally neglected. The expression of the drag force experienced by an isolated particle in an infinite domain is well known and was derived theoretically and empirically for Stokes and inertial flows, respectively. This force is not only dependent on the relative velocity between the fluid and the particle but also on the presence of surrounding particles. The influence of surrounding particles is often expressed by the local fluid volume fraction $\mathcal{E}_f$. So far, there exists neither a theoretical formula nor accurate correlation that describes faithfully the drag force intensity in moderately dense to dense suspensions and any flow regimes. However, several expressions were proposed in the literature with various domains of validity in terms of particle Reynolds number Re_p and fluid volume fraction $\mathcal{E}_f$. In a fluidized bed, the solid concentration varies from close packing ($1 - \mathcal{E}_f \approx 0.6$) to dilute regime ($1 - \mathcal{E}_f \lesssim 0$) in relation to the fluid bubbles/particles clusters dynamics. Hence, the drag force correlation is required to be reliable on a wide range of $\mathcal{E}_f$. The classical approach to construct such a reliable closure law is to combine Wen and Yu's correlation[13] for dilute regimes to Ergun's correlation[14] for dense regimes. The former is derived by multiplying an infinitely dilute drag force formula by a function of $\mathcal{E}_f$ while the latter is based on a porous media assumption. The threshold to switch from Wen and Yu's correlation to Ergun's correlation and vice versa is generally set to $\mathcal{E}_f = 0.8$. Over the years, many other correlations were suggested in the literature. For instance, to extend the range of validity of Wen and Yu's correlation to the full $\mathcal{E}_f$ range, Di Felice[15] suggested an improvement based on experimental results that has been widely adopted by the community. In Wen and Yu's correlation, the presence of surrounding particles is accounted for by a constant power of $\mathcal{E}_f$. In Di Felice's improved model, the power of $\mathcal{E}_f$ is not a constant anymore but a function of Re_p and $\mathcal{E}_f$ itself. For many years, experiments were the most reliable source of data (assuming measurement uncertainty is controlled) to derive drag force closure laws. However, measurement techniques can be intrusive, and detailed information in the core of the flow in a (generally fixed) bed is not necessarily easy to extract. A more recent alternative is microscale simulation that supplies detailed information to derive new drag force correlations. As an example, Hill and Koch performed many lattice-Boltzmann microscale simulations on a wide range of $\mathcal{E}_f$ and suggested two drag force correlations, the former for low Reynolds number flows[16] and the latter for moderate Reynolds number flows.[17] These two correlations have then been employed by several other research teams. The correlations were even further improved by the group of Kuipers that suggested another correlation[18] also often used in the community.[6,19,20]

The aim of this paper is not to derive yet another drag law correlation. Our goal is to discuss the numerical implementation of our DEM-CFD model and examine the influence of various numerical and geometric parameters on the computed results produced by such a numerical model. Looking at the broad literature on DEM-CFD simulations, our impression is that many papers do not detail enough their numerical implementation and the selected values of the associated numerical parameters. This inevitably leads to significant variations of bed dynamics and impedes a proper comparison between different works. From a physical viewpoint, the influence of tangential friction on fluidized bed dynamics has not yet received a large amount of attention, and we intend with this work to contribute to filling that gap in the literature.

The rest of the paper is organized as follows. Section 2 gives the set of volume-averaged Navier−Stokes equations describing the fluid phase, the DEM/soft sphere model used to compute collisions, and the interphase coupling terms. We present the numerical implementation of the model and dedicate particular attention to the Lagrangian−Eulerian projection operator used for interphase coupling. Using statistical analysis tools, we investigate in Section 3 the dependence of bubbling fluidized bed dynamics to the following numerical parameters: solid time-step magnitude, fluid time-step magnitude, and fluid grid

DOI: 10.1021/acs.iecr.6b03627

size to particle diameter ratio, and to the size of the domain in the biperiodic configuration adopted. In Section 4, we perform validation tests on two different fluidized bed configurations, a bubbling fluidized bed and a semi-3D spouted fluidized bed, i.e., a spouted bed whose depth spans a few particle diameters only, to further assess the consistency of the model and the validity of the implementation. Finally, we perform in Section 5 simulations of the same semi-3D spouted bed with different values of the Coulomb friction coefficient to investigate the quantitative impact of tangential friction on the dynamics of the spouted bed. A conclusion together with perspectives is given in Section 6.

2. EQUATIONS OF THE MODEL

We present below the governing equations of the model, i.e., conservation equations and closure laws, and detail their numerical implementation. The surrounding fluid is assumed to be Newtonian with viscosity μ_f and to have a constant density ρ_f.

2.1. Computational Fluid Dynamics. In a way similar to the TFM, the fluid phase is governed by the volume-averaged Navier–Stokes equations. Control volumes ΔV are at least an order of magnitude larger than the particle volume V_p. The mass and momentum equations are solved on the actual volume occupied by the fluid. This leads to the classical $\mathcal{E}_f$-weighted formulation of the mass and momentum equations as follows:

$$\begin{cases} \dfrac{\partial}{\partial t}(\varepsilon_f \rho_f) + \nabla\cdot(\varepsilon_f \rho_f \boldsymbol{u}_f) = 0 & \text{(1a)} \\ \dfrac{\partial}{\partial t}(\rho_f \varepsilon_f \boldsymbol{u}_f) + \nabla\cdot(\rho_f \varepsilon_f \boldsymbol{u}_f \boldsymbol{u}_f) = -\nabla p + \boldsymbol{F}_{pf} + \nabla\cdot(\varepsilon_f \boldsymbol{\tau}_f) & \text{(1b)} \end{cases}$$

where $\boldsymbol{u}_f$ denotes the fluid velocity. The momentum equation (eq 1b) does not contain any gravity term, and hence, the pressure p represents the hydrodynamic pressure, i.e., the total pressure minus the hydrostatic pressure contribution. Consequently, the buoyancy force exerted on particles is explicitly accounted for in Newton's equations such that particles are subjected to the right net weight (Section 2.2). At the microscale, the stress tensor $\boldsymbol{\tau}_f$ of an incompressible Newtonian fluid reads as follows:

$$\boldsymbol{\tau}_f = \mu_f(\nabla \boldsymbol{u}_f + \nabla \boldsymbol{u}_f^t) = 2\mu_f \boldsymbol{D} \tag{2}$$

where $\boldsymbol{D} = \frac{1}{2}(\nabla \boldsymbol{u}_f + \nabla \boldsymbol{u}_f^t)$ is the rate-of-strain tensor. Here, $\boldsymbol{F}_{pf}$ represents the particles to fluid interphase momentum transfer. The pressure gradient is not multiplied by ε_f in the momentum equation (eq 1b); thus, this set of equations corresponds to the so-called model B in the literature.[5] An alternative formulation of the model is the so-called model A in which the pressure gradient is also weighted by ε_f. These two formulations lead to slightly different expressions for the interphase momentum transfer (with or without an explicit contribution of the pressure gradient). Both formulations are self-consistent and have led to long discussions in the literature (see, e.g.,refs 10–12, 21–23). There are no significant differences in the performance of the two model formulations,[21] although some authors favored model B as more prone to yield accurate results at low fluidization velocity.[12] In this work, we use model B.

As fluid density ρ_f and fluid viscosity μ_f are assumed to be constant, the system of eqs 1 can be rewritten as follows:

$$\begin{cases} \dfrac{\partial \varepsilon_f}{\partial t} + \nabla\cdot(\varepsilon_f \boldsymbol{u}_f) = 0 & \text{(3a)} \\ \rho_f\left(\dfrac{\partial}{\partial t}(\varepsilon_f \boldsymbol{u}_f) + \nabla\cdot(\varepsilon_f \boldsymbol{u}_f \boldsymbol{u}_f)\right) = -\nabla p + \boldsymbol{F}_{pf} + 2\mu_f \nabla\cdot(\varepsilon_f \boldsymbol{D}) & \text{(3b)} \end{cases}$$

We discretize eqs 3 with a classical Finite Volume/Staggered Grid scheme on a Cartesian grid. Pressure and fluid volume fraction are located at the center of each computational fluid cell. Fluid velocity components are defined at cell face centers as follows: u_i is defined at the center of the cell face perpendicular to x_i, i = 1, 2, 3. The system of eqs 3 is solved in time by a first-order Marchuk–Yanenko operator-splitting solution algorithm[24,25] in the spirit of a pseudo-L^2 projection method. Introducing a constant time step Δt_f and knowing the solution at time $t^n = n\Delta t_f$ and $t^{n-1} = (n-1)\ \Delta t_f$, the solution at time $t^{n+1} = (n+1)\ \Delta t_f$ is obtained through the following sequence of subproblems:

1. We first solve the following advection-diffusion problem:

$$\begin{aligned} &\rho_f \frac{\varepsilon_f^n \boldsymbol{u}_f^* - \varepsilon_f^{n-1}\boldsymbol{u}_f^n}{\Delta t_f} - 2\mu_f \nabla\cdot(\varepsilon_f^n \boldsymbol{D}(\boldsymbol{u}_f^*)) \\ &\quad = -\boldsymbol{F}_{pf}^n - \rho_f \nabla\cdot(\varepsilon_f^{n-1}\boldsymbol{u}_f^n \boldsymbol{u}_f^n) \end{aligned} \tag{4}$$

   where $\boldsymbol{u}_f^*$ stands for the velocity field at the intermediate stage. Note that in eq 4, the viscous term 2 μ_f $\nabla\cdot(\varepsilon_f^n$ $\boldsymbol{D}(\boldsymbol{u}_f^*))$ is treated implicitly and the explicit treatment of the advection term $\rho_f \nabla\cdot(\varepsilon_f^{n-1}$ $\boldsymbol{u}_f^n$ $\boldsymbol{u}_f^n)$ requires us to satisfy a CFL stability condition.
2. We then impose mass conservation through the solution of a Stokes-like problem as follows:

$$\begin{cases} \rho_f \dfrac{\varepsilon_f^n \boldsymbol{u}_f^{n+1} - \varepsilon_f^n \boldsymbol{u}_f^*}{\Delta t_f} = -\nabla p^{n+1} & \text{(5a)} \\ \dfrac{\varepsilon_f^n - \varepsilon_f^{n-1}}{\Delta t_f} + \nabla\cdot(\varepsilon_f^n \boldsymbol{u}_f^{n+1}) = 0 & \text{(5b)} \end{cases}$$

In eq 44, the viscous term 2 μ_f $\nabla\cdot(\varepsilon_f^n$ $\boldsymbol{D}(\boldsymbol{u}_f^*))$ and the advection term $\rho_f \nabla\cdot(\varepsilon_f^{n-1}$ $\boldsymbol{u}_f^n$ $\boldsymbol{u}_f^n)$ are discretized in space with a classical second order accurate centered scheme and a second order accurate TVD/Superbee limiter scheme, respectively (see ref 26 among others).

2.2. Discrete Element Model. In DEM modeling, particles position and velocity are known for each individual particle and particles are tracked in a Lagrangian way.[27] In this work, we assume that all particles are spherical. The linear and angular motion of a (spherical) particle is given by the Newton's second law as follows:

$$\begin{cases} m_p \dfrac{d\boldsymbol{v}_p}{dt} = m_p \boldsymbol{g} + \boldsymbol{f}_{pp} + \boldsymbol{f}_{fp} & \text{(6a)} \\ \boldsymbol{I}_p \dfrac{d\boldsymbol{\omega}_p}{dt} = \boldsymbol{T}_{pp} + \boldsymbol{T}_{fp} & \text{(6b)} \end{cases}$$

where $m_p = \rho_p\ \pi d_p^3/6$ is the particle mass, ρ_p the particle density, d_p the particle diameter, $\boldsymbol{I}_p = i_p \boldsymbol{I}$ the particle moment of inertia tensor, $\boldsymbol{I}$ the identity tensor, $i_p = \rho_p\ \pi d_p^5/60$ the diagonal coefficient of $\boldsymbol{I}_p$, $\boldsymbol{g}$ the gravity acceleration, $\boldsymbol{v}_p$ the particle translational velocity, and $\boldsymbol{\omega}_p$ the particle angular velocity. Here, $\boldsymbol{f}_{pp}$ is the total particle–particle and wall–particle contact (also denoted as collision) force acting on the particle, and $\boldsymbol{f}_{fp}$ is the total fluid–particle hydrodynamic interaction force. Also $\boldsymbol{T}_{pp}$ and $\boldsymbol{T}_{fp}$ denote the total contact torque and the total hydro-

DOI: 10.1021/acs.iecr.6b03627

dynamic torque, respectively. To solve the system of eqs 6, we need a model for the contact contribution $(\boldsymbol{f}_{pp},\boldsymbol{T}_{pp})$ as well as a model for the hydrodyamic contribution $(\boldsymbol{f}_{fp},\boldsymbol{T}_{fp})$.

The binary hard sphere model and soft sphere model are the two categories of collision models generally used for particulate flows.[28] For the former, the whole momentum exchange between two colliding particles takes place exactly at the time when the two particles touch each other. Thus, contacts are instantaneous, and even if a particle is colliding with more than one neighboring particle, contacts must be treated one after another, i.e., in a binary way. In contrast, for the latter, particles overlap slightly (Figure 1) such that a contact lasts a few time

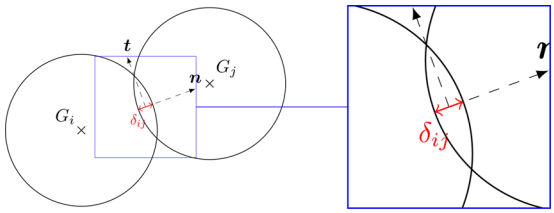

Figure 1. Contact between two particles: G_i and G_j denote the centers of mass of particles i and j, respectively, M the contact point, $\boldsymbol{n}$ and $\boldsymbol{t}$ the unit normal and tangential vectors at the contact point, respectively, and δ_{ij} the overlapping distance.

steps and that collision forces are function of overlap distance δ_{ij} and relative velocity $\boldsymbol{v}_r$ between two colliding particles. Then, contacts between a given particle and its colliding neighbors can be integrated in time all together.

In our DEM granular solver,[29,30] the total collision force comprises the following terms:

- An elastic restoring force

$$\boldsymbol{f}_{el} = k_n \delta_{ij} \boldsymbol{n}_{ij} \tag{7}$$

in the normal direction where k_n denotes the normal contact stiffness, δ_{ij} the overlapping distance between particles i and j, and $\boldsymbol{n}_{ij}$ the unit normal vector between particles i and j centers of mass.

- A viscous dynamic force

$$\boldsymbol{f}_{dn} = -2\gamma_n m_{ij} \boldsymbol{v}_{rn,ij} \tag{8}$$

in the normal direction to account for the dissipative nature of the contact, where γ_n is the normal dynamic friction coefficient, $m_{\mathrm{ij}} = \frac{M_i M_j}{M_i + M_j}$ the reduced mass of particles i and j, and $\boldsymbol{v}_{rn,ij}$ the normal relative velocity between particles i and j.

- A tangential friction force

$$\boldsymbol{f}_t = -\min\{\mu_C |\boldsymbol{f}_{el}|, |\boldsymbol{f}_{dt}|\} \boldsymbol{t}_{ij} \tag{9}$$

$$\boldsymbol{f}_{dt} = -2\gamma_t m_{ij} \boldsymbol{v}_{rt,ij} \tag{10}$$

where $\boldsymbol{f}_{dt}$ denotes the dissipative frictional contribution, γ_t the dissipative tangential friction coefficient, $\boldsymbol{v}_{rn,ij}$ the tangential relative velocity between particles i and j, and $\boldsymbol{t}_{\mathrm{ij}}$ the unit tangential vector. Note that the magnitude of the tangential friction force is limited by the Coulomb frictional limit calculated with the Coulomb dynamic friction coefficient μ_C.

The total collision force acting on a particle i is the sum of contributions related to the contact with neighboring particles j and walls w:

$$\begin{aligned} \boldsymbol{f}_{pp,i} &= \sum_j \boldsymbol{f}_{pp,ij} + \sum_w \boldsymbol{f}_{pp,iw} \\ &= \sum_j (\boldsymbol{f}_{el} + \boldsymbol{f}_{dn} + \boldsymbol{f}_t)_{ij} + \sum_w (\boldsymbol{f}_{el} + \boldsymbol{f}_{dn} + \boldsymbol{f}_t)_{iw} \end{aligned} \tag{11}$$

Since for a sphere the radial vector $\boldsymbol{R}_{ij}$ from particle i center of mass to the point of contact with particle j is always colinear to the unit normal vector $\boldsymbol{n}_{ij}$, only the tangential contact force contributes to the contact torque (same applies for a contact with a wall). The corresponding total collision torque for spheres hence reads as follows:

$$\boldsymbol{T}_{pp,i} = \sum_j \boldsymbol{R}_{ij} \wedge \boldsymbol{f}_{t,ij} + \sum_w \boldsymbol{R}_{iw} \wedge \boldsymbol{f}_{t,iw} \tag{12}$$

The Lagrangian tracking of all particles with collisions is computed by our in-house massively parallel DEM solver Grains3D.[29] In this DEM code, we solve Newton's eqs 6 in time with a second order time-accurate leapfrog scheme. Thus, particles linear and angular velocity $(\boldsymbol{v}_p,\boldsymbol{\omega}_p)$ and position $(\boldsymbol{x}_p,\boldsymbol{\theta}_p)$ are computed in the following way:

$$\begin{aligned} \boldsymbol{v}_p(t + \Delta t_p/2) &= \boldsymbol{v}_p(t - \Delta t_p/2) + \frac{\sum \boldsymbol{f}(t)}{m_p} \Delta t_p \\ \boldsymbol{\omega}_p(t + \Delta t_p/2) &= \boldsymbol{\omega}_p(t - \Delta t_p/2) + \frac{\sum \boldsymbol{T}(t)}{i_p} \Delta t_p \end{aligned} \tag{13}$$

$$\begin{aligned} \boldsymbol{x}_p(t + \Delta t_p) &= \boldsymbol{x}_p(t) + \boldsymbol{v}_p(t + \Delta t_p/2) \Delta t_p \\ \boldsymbol{\theta}_p(t + \Delta t_p) &= \boldsymbol{\theta}_p(t) + \boldsymbol{\omega}_p(t + \Delta t_p/2) \Delta t_p \end{aligned} \tag{14}$$

where Δt_p denotes the solid time step. Note that the integration of $\boldsymbol{\theta}_p$ as written above is only formal. In practice, it involves rotation matrices or quaternions. Grains3D can compute collisions between particles of arbitrary convex shape. In fact, the collision detection strategy is based on a Gilbert–Johnson–Keerthi (GJK) distance algorithm.[31] However, for spheres, the contact detection (contact point and overlap distance) relies on an analytical formula (Figure 1). This remarkably speeds up contact detection. To accelerate even more contact detection, a classical linked-cell spatial sorting[32] is used to identify particles that potentially collide. More details about the granular solver Grains3D can be found in.[29]

2.3. Action of the Fluid on Particles.

Following the classical DEM-CFD models in the literature, we neglect the hydrodynamic torque $\boldsymbol{T}_{fp}$ in eq 6b. This implies that particles angular motion is due to collisions only. The fluid–solid interaction force $\boldsymbol{f}_{fp}$ derives from integration of the fluid stress tensor over the particle surface and requires to be closed. In this study, we assume that dominant hydrodynamic forces are buoyancy force and drag force. The added mass force and the Basset force are assumed to be negligible due to the high solid/fluid density ratio and the low fluid viscosity considered later on in this work. Finally, we neglect the Saffman lift force and the Magnus lift force for the two following primary reasons: (i) to be coherent with the assumption $\boldsymbol{T}_{fp} = \boldsymbol{0}$ as these two forces imply fluid-induced particle rotation and (ii) the lack of reliable correlations in the literature at high solid volume fraction/low ε_f (hindrance effect). Thus, the force exerted by the fluid on each individual particle is

$$\boldsymbol{f}_{fp} = -\rho_f V_p \boldsymbol{g} + \boldsymbol{f}_D \tag{15}$$

DOI: 10.1021/acs.iecr.6b03627

where $-\rho_f V_p \boldsymbol{g}$ corresponds to buoyancy force and $\boldsymbol{f}_D$ to drag force. Several drag force expressions have been suggested in the literature depending on the flow regime characterized by particle Reynolds number Re_p and local fluid volume fraction ε_f. All these expressions can be written in the following form:

$$\boldsymbol{f}_D = V_p \frac{\beta}{\varepsilon_f(1-\varepsilon_f)}(\boldsymbol{u}_f - \boldsymbol{v}_p) \tag{16}$$

where β denotes the interphase momentum transfer coefficient. The presence of $1/\varepsilon_f$ in the denominator is specific to model B. Indeed, coefficients β in model A and model B are related to each other by the following formula: $\beta_B = \beta_A / \varepsilon_f$.[5] In process engineering, the most commonly used expression of this coefficient is a combination of Wen and Yu's equation for low particle concentration (high ε_f, dilute regime)[13] to Ergun's equation for moderate to high particle concentration (low ε_f, dense regime):[14]

$$\beta_{\text{Ergun}} = 150\frac{(1-\varepsilon_f)^2\mu_f}{\varepsilon_f d_p^2} + 1.75\frac{(1-\varepsilon_f)\rho_f}{d_p}|\boldsymbol{u}_f - \boldsymbol{v}_p| \tag{17}$$

$$\beta_{\text{Wen\&Yu}} = \frac{3}{4}C_D\frac{(1-\varepsilon_f)\varepsilon_f}{d_p}|\boldsymbol{u}_f - \boldsymbol{v}_p|\varepsilon_f^{-2.65} \tag{18}$$

where the drag coefficient C_D is given by the Schiller–Naumann correlation[33] as follows:

$$C_d = \begin{cases} \frac{24}{Re_p}(1 + 0.15Re_p^{0.687}) & Re_p < 1000 \\ 0.44 & Re_p \geqslant 1000 \end{cases} \tag{19}$$

where the particle Reynolds number Re_p is defined as

$$Re_p = \frac{\rho_f d_p \varepsilon_f |\boldsymbol{u}_f - \boldsymbol{v}_p|}{\mu_f} \tag{20}$$

To avoid any discontinuity between eqs 17 and 18, Huilin and Gidaspow[34] introduced an additional function that smoothes out the transition from low to high ε_f regimes.

$$\varphi_{\text{Huilin}} = \frac{\tan^{-1}(150 \times 1.75(0.2 - (1-\varepsilon_f)))}{\pi} + 0.5 \tag{21}$$

$$\beta_{\text{Huilin}} = (1-\varphi_{\text{Huilin}})\beta_{\text{Ergun}} + \varphi_{\text{Huilin}}\beta_{\text{Wen\&Yu}} \tag{22}$$

Over the past 20 years, other correlations reasonably valid for a wide range of Re_p and ε_f were suggested in the literature.[15,17,18,35] Among others, the expression proposed by Beetstra et al.[18] seems to perform quite well:

$$\beta_{\text{Beetstra}} = \frac{18\mu_f\varepsilon_f(1-\varepsilon_f)}{d_p^2}(F_1 + F_2) \tag{23}$$

with

$$F_1 = \frac{10(1-\varepsilon_f)}{\varepsilon_f^2} + \varepsilon_f^2(1 + 1.5\sqrt{1-\varepsilon_f}) \tag{24}$$

$$F_2 = \frac{0.413Re_p}{24\varepsilon_f^2}\cdot\frac{\varepsilon_f^{-1} + 3\varepsilon_f(1-\varepsilon_f) + 8.4Re_p^{-0.343}}{1 + 10^{3(1-\varepsilon_f)}Re_p^{-2.5-\varepsilon_f}} \tag{25}$$

In this work, simulations are performed with the expression of Huilin and Gidaspow[34] or the expression of Beetstra et al.[18] As plotted in Figure 2, different drag correlations predict

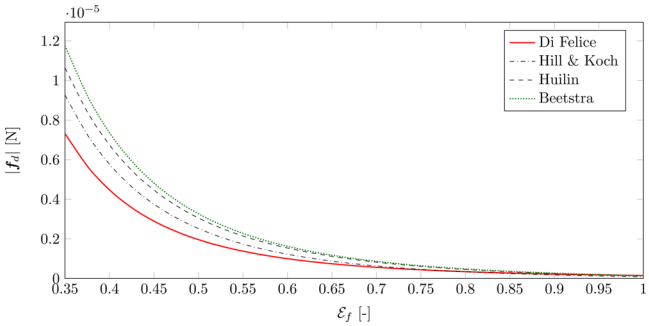

Figure 2. Drag force depending on the fluid volume fraction for a particle of diameter $d_p = 10^{-3}$ m with a relative velocity $|\boldsymbol{u}_f - \boldsymbol{v}_p| = 0.35$ m/s in air ($\rho_f = 1.2$ kg/m^3, $\mu_f = 1.8$ Pa s). Correlations proposed by Di Felice,[15] Hill and Koch,[17] Huilin,[34] and Beetstra.[18]

significantly different values of the drag force for low ε_f (dense regime), while they generally agree with each other for high ε_f (dilute regime).

2.4. Action of Particles on the Fluid. According to Newton's third law of motion (action–reaction principle), momentum transfer from solid phase to fluid phase should be equal to the one from fluid phase to solid phase but with opposite sign. This equality has to be satisfied at a global level as much as at the local level, i.e., in each cell of the computational fluid domain. Note that for consistency with the form of eq 1b without any gravity term, there is no contribution of the buoyancy force in the action of the particles on the fluid.

When a particle belongs to a single computational fluid cell, its total drag force $\boldsymbol{f}_d$ contributes to $\boldsymbol{F}_{pf}$ in that cell. However, when a particle overlaps several fluid cells, the contribution of its drag force $\boldsymbol{f}_d$ must be shared between (projected onto) the cells it belongs to. Here, $\boldsymbol{F}_{pf}$ represents a source term in the momentum equation (eq 3b) and is computed explicitly before each fluid solver iteration. It models the particles feedback effect or particles reaction on the fluid. Here, we use a simple projection operator based on the fraction of the particle belonging to a control volume. Hence, $\boldsymbol{F}_{fp}$ is computed as follows:

$$\boldsymbol{F}_{pf} = \frac{1}{V_k^{CV}}\sum_i \theta_{i,k}\boldsymbol{f}_{D,i} \tag{26}$$

where $\theta_{i,k}$ is a measure of the fraction of particle i in control volume k. The computational details to estimate $\theta_{i,k}$ are given in Section 2.5. With the Finite Volume/Staggered Grid discretization scheme used in this study, the projection of $\boldsymbol{f}_d$ to compute $\boldsymbol{F}_{pf}$ is performed for each velocity component separately as each velocity component is defined on a different control volume (staggered layout of the velocity components).

2.5. Projection Operator from Lagrangian to Eulerian. We detail here how we project Lagrangian quantities on the Eulerian grid and illustrate the method on the computation of the fluid volume fraction ε_f. The same projection operator is used to project the hydrodynamic Lagrangian forces $\boldsymbol{f}_d$ on the Eulerian grid to compute the source term $\boldsymbol{F}_{pf}$ (particles reaction of the fluid) in the momentum equation. The projection operator is a key component of the interphase coupling. For instance, the drag force acting on a particle is highly dependent

DOI: 10.1021/acs.iecr.6b03627

on the fluid volume fraction ε_f (Figure 2); hence, an as accurate as possible computation of ε_f is crucial. The fluid grid size is controlled by two somehow contradictory constraints: (i) A fluid grid cell volume ΔV needs to be an order of magnitude larger that a particle volume for the averaging process to be sensible, i.e.,

$$\Delta V \geq 10 V_p \tag{27}$$

(ii) The smaller the grid size is, the more accurate the fluid flow features are captured.

An intuitive method to compute the fluid volume fraction ε_f in each cell depending on the presence of the particles has been proposed by Hoomans et al.:[8]

$$\varepsilon_f = 1 - \frac{1}{V_j^{CV}} \sum_i \theta_{i,j} V_{p,i} \tag{28}$$

where $\theta_{i,k}$ is the portion of particle i in cell k (similarly to $\boldsymbol{F}_{fp}$ in eq 26).

In two dimensions, the calculation of $\theta_{i,j}$ is straightforward using geometrical considerations, and an analytical formula is available for the intersected surface area of a disc and a rectangle. In three dimensions, it is much more difficult to calculate the exact portion of the particle volume that belongs to each cell when this particle straddles several fluid cells (maximum 8 cells if condition 27 is satisfied). Actually, no analytical formula exists for the intersected volume of a sphere and a box. Different techniques have been used to circumvent this problem. The simplest technique, called the *center particle method*, assumes that a particle can only be either fully inside or fully outside a cell, depending on the position of its center of mass. It is an extremely fast computing way of approximating ε_f but presents two drawbacks. First, its accuracy is extremely low and can lead to a totally wrong approximation of ε_f as illustrated in Figure 3. Second, ε_f time variations are not smooth because

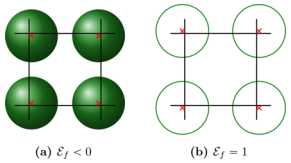

Figure 3. Examples of particles/cell configurations illustrating the wrong evaluation of the fluid volume fraction by using the Particle Center Method.

of the sudden consideration of a particle in a cell (out at t^{n-1} and in at t^n). This jump leads to spurious oscillations, especially due to the presence of the fluid volume fraction ε_f time-derivative term in the degenerated Stokes problem (eq 5). The *center particle method* does not satisfy the basic time-step convergence property, and we have instead

$$\lim_{\Delta t \to 0} \frac{\varepsilon_f^n - \varepsilon_f^{n-1}}{\Delta t} = \pm\infty \tag{29}$$

For finite Δt, it also performs worse and worse as the fluid grid size decreases (since the particle volume is finite, $\Delta\varepsilon_f = \varepsilon_f^n - \varepsilon_f^{n-1}$ increases as the fluid grid size decreases), hence impacting the overall space convergence of the numerical method too.

In order to improve the fluid volume fraction ε_f calculation, other methods were suggested in the literature as, e.g., the *offset method* of Alobaid et al.,[19] the *porous cube method* of Link et al.,[36,37] or more recently, the interesting *mollification kernel/Gaussian filtering method* of Pepiot and Desjardins.[6] The method we adopt in this work derives from the porous cube method proposed by Link et al. and assumes that the portion of the particle i belonging to a control volume k, i.e., $\theta_{i,k}$, can be approximated by the intersected volume of the smallest cube embedding the particle i (a cube whose edge length is equal to the particle diameter) and the control volume k.

$$\theta_{i,k} = \frac{V_k^{\text{approx}}}{V_{\text{cube},i}} \tag{30}$$

where $V_{\text{cube},i} = d_p^3$ is the volume of the cube embedding the spherical particle i and V_k^{approx} is the intersected volume of the cube with the fluid cell k. Figure 4a shows the methodology in a 2D case, the extension to 3D is straightforward.

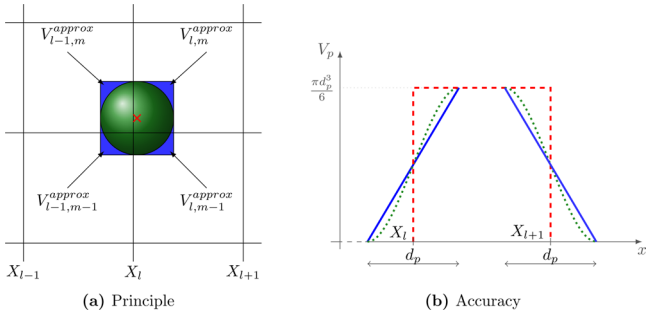

Figure 4. Our embedding cube/square approximation method: (a) principle and (b) accuracy of the approximation as the evolution of particle volume crossing control volume l: (green dots) disc analytic solution, (blue line) our embedding square approximation method, (red dotted line) particle center method.

Our method smoothes out the calculation of the ε_f time-derivative term in the degenerated Stokes problem (eqs 5) and recovers time convergence. This is a very important property. It also permits to use a smaller grid size than the *particle center method*, i.e., down to $\Delta V \simeq 6V_p$, while yielding a reasonably accurate approximation of ε_f as illustrated in Figure 4b.

2.6. Space/Time Complexity and Computing Performance. Bubbling and spouted fluidized beds are generally considered as moderately dense to dense fluid/particles systems. In fact, the average porosity ε_f is ≈ 0.7 in the bed (i.e., the solid volume fraction is $\approx 0.3 = 30\%$). Hence, the major part of the computing time as well as the space/time complexity of our DEM-CFD model is related to particles. The time complexity of particles motion is simply $O(N_s)$, where N_s is the total number of solid time steps performed over a simulation. The Lagrangian particle tracking and the computation of the hydrodynamic force $\boldsymbol{f}_{fp}$ exerted on each particle scale linearly with the total number of particles N_p, i.e., $O(N_p)$. The computation of particles collisions theoretically scales as $O(N_p^2)$, but the use of a linked-cell spatial sorting reduces the space complexity to $O(13N_cN_p)$, where N_c is the average number of particles per linked cell. In fluidized bed simulations, $N_c \approx 1$, such that the space complexity of particles collisions computation is $O(13N_p)$. The overall space/time complexity of particles motion is thus formally $O(15N_pN_s)$ (we say "formally", as the constant 15 is not necessarily relevant). The projection operator scales linearly with N_p. The corresponding space complexity is bounded by $O(8N_p)$ as a particle overlaps eight fluid cells at most. The projection operator is used both for

DOI: 10.1021/acs.iecr.6b03627

porosity and the three components of the velocity; hence, the space complexity is bounded by $O(32N_p)$. As the projection operator is used once per fluid time step, the overall space/time complexity of our DEM-CFD model is $O(15N_pN_s+32N_pN_f)$, where N_f is the total number of fluid time steps performed over a simulation. Introducing the integer ratio of fluid time-step magnitude over solid time-step magnitude $r_N = \Delta t_f/\Delta t_p$, the space/time complexity of our DEM-CFD model can be formally rewritten as $O((15 + 32/r_N)\ N_pN_s)$. Dropping the prefactor $15 + 32/r_N$, the space/time complexity of our DEM-CFD model is essentially $O(N_pN_s)$.

The model presented previously has been implemented in the fully MPI platform PeliGRIFF[38] in order to simulate systems containing up to a few tens of millions of particles. For fluidized beds and simple box geometries, a 2D domain decomposition in the horizontal plane $x-y$ (assuming gravity and inlet velocity are in the vertical direction z) and a similar domain decomposition for fluid domain and particles domain supplies the best parallel performance. In fact, it guarantees a reasonably constant particle load balancing over time and significantly reduces the number of proc-to-proc (i.e., subdomain-to-subdomain) communications. Each subdomain slightly overlaps with its neighboring subdomains by (i) two layers of fluid grid cells to properly assemble all terms in the fluid conservation equations (and, in particular, the advection term with the second order TVD scheme) and (ii) a single layer of cells of the linked-cell grid to detect collisions with particles located in a neighboring subdomain.

Several simulations are performed on different configurations in order to study the parallel scalability of our numerical implementation. As we are interested in large-scale simulations, we evaluate the parallel scalability with weak scaling tests only. In other words, we set up the system in terms of a constant load per node, and we record the computing time as a function of the number of nodes with the size of the system increasing accordingly in the horizontal directions (which means that the height of the domain is constant while the cross section increases with the number of nodes). We present below results of a representative scalability test for a homogeneous bubbling fluidized bed. Features of the system are as follows:

- Inlet velocity at the bottom wall is constant in space and in time and is set to $U_{in} = 3U_{mf}$.
- Boundary conditions on the lateral (vertical) boundaries are biperiodic.
- Each subdomain (i.e., core) has a size of $20d_p \times 20d_p \times 200d_p$.
- Grid size is set to $\Delta x = 2.5d_p$, and hence, each subdomain (i.e., core) contains $8 \times 8 \times 80 = 5120$ fluid cells.
- Each subdomain (i.e., core) contains at the initial time $20 \times 20 \times 200 = 80{,}000$ spherical particles.
- Our jobs run on a 16-core per node supercomputer, so the reference for the weak scaling test is a full node, i.e., a simulation on 16 cores with $16 \times 80{,}000 = 1{,}280{,}000$ particles and $16 \times 5{,}120 = 81{,}920$ fluid cells.

An ideal scalability means that the computing time is constant as the domain size and number of nodes increase simultaneously. Figure 5 shows the evolution of the computing time spent in each part of the code as a function of the number of nodes/system size. For the granular solver, we observe that after a rise of 5% between 1 and 2 nodes as a result of the internode communication overhead mainly related to the supercomputer architecture, the computing time keeps being

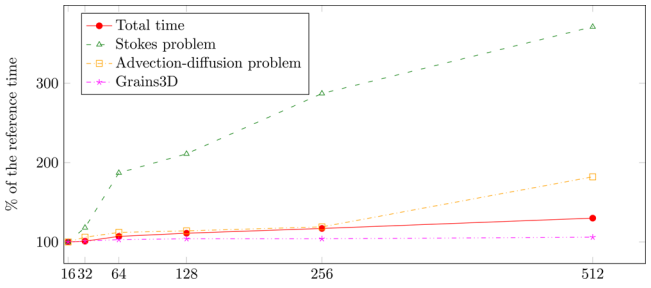

Figure 5. Scaling performance for a constant load per core (80,000 particles/5120 fluid cells). Evolution of the computational time spent in the various parts of the code as a function of the number of cores normalized by the time spent on a full node (16 cores).

quasi-constant up to 32 nodes (i.e., 512 cores and 40,960,000 particles). This emphasizes the highly satisfactory parallel scalability of the granular solver. Concerning the fluid solver, the advection−diffusion problem scales quite well up to 16 nodes/256 cores and then a little less satisfactorily at 32 nodes/512 cores. The decay of the scalability of the advection−diffusion problem solution over 16 nodes/256 cores is not entirely clear and is currently investigated in our group. It could be related to many diverse causes (as, e.g., the supercomputer network architecture on which jobs were run that groups 18 nodes together in a chassis; a 16 nodes job uses a single chassis of nodes, while a 32 nodes requires two chassis, and interchassis communication may cause an additional overhead) that are beyond the scope of this paper. The Stokes problem solution scales quite poorly as the number of nodes/cores increases. In fact, the computing time increases a lot from 1 node to 32 nodes. This was however predictable as the number of fluid cells per subdomain is rather low (due to the fluid grid size constraint (eq 27), and the Stokes problem involves the solution of a pressure Poisson problem solved in our code by an algebraic multigrid conjugate gradient method. It is known that the scalability of the multigrid method (or more generally any iterative solver) decays as the number of nodes/cores increases if the number of fluid cells (pressure unknowns) per core is too small. This has been verified by increasing the number of fluid cells per core in the horizontal direction from $8 \times 8 \times 80 = 5120$ to $32 \times 32 \times 80 = 81{,}920$. In fact, Figure 6 clearly highlights that the multigrid solver for the pressure Poisson problem performs better and better in terms of parallel scalability as the load of fluid cells per core increases. Obviously, since a $32 \times 32 \times 80$ subdomain now hosts 16 times more particles, the total computing time increases accordingly although the parallel scalability improves. However, even with a $8 \times 8 \times 80$ subdomain, the overall parallel scalability is rather satisfactory. In fact, the red line in Figure 5 indicating the total computing time increase for a given number of nodes with respect to a single node shows a linear trend with a very small slope. For 32 nodes/512 cores/40,960,000 particles/2,621,440 fluid cells, this increases is around 30% only, i.e., a parallel scalability of $100/130 \simeq 0.77$. On the basis of this weak scaling test, we believe that configurations similar to our representative test (fluidized beds in a box geometry) in which dynamic load balancing is not required can easily be simulated with our code with up to a few hundreds of millions of spherical particles on a few thousands of cores with a good parallel scalability, i.e., larger than 0.7, provided the load of particles per core is of the order of 10^5.

DOI: 10.1021/acs.iecr.6b03627

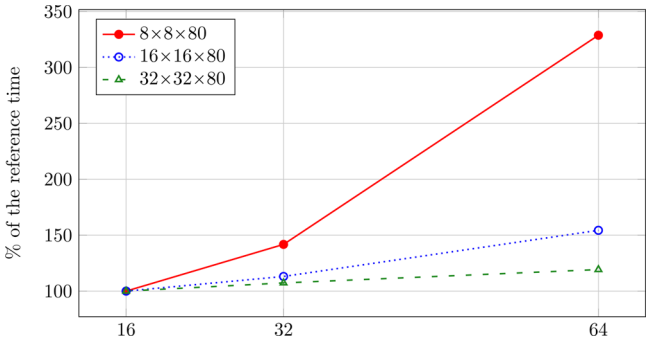

Figure 6. Evolution of the scaling performace for the solution of the Stokes problem as a function of the number of cores for different fluid cells loads per core. The reference is the time spent on a full node (16 cores).

3. SENSITIVITY OF THE MODEL TO NUMERICAL AND GEOMETRIC PARAMETERS IN THE CASE OF BUBBLING FLUIDIZED BEDS

As many variants of the two-way Euler−Lagrange model exist as, e.g., formulations A and B,[39] contact solver, fluid flow solver, we would like to provide here a clear and detailed validation and sensitivity survey of our model that any other group can reproduce. In this section, we consider bubbling fluidized beds without wall effects. We first define statistical tools to analyze the bed dynamics. Then, we examine the influence of the following numerical parameters: solid time-step magnitude, fluid time-step magnitude, and fluid grid size on the computed solution as well as the influence of the geometric size of the domain in controlling the bubbling dynamics of the system.

3.1. Bed Statistics. A three-dimensional fluidized bed generally comprises a large number of particles and exhibits a highly unsteady dynamics. As a result, the system can be characterized in terms of statictics only. It is hence crucial to define relevant statistical markers of the flow and a criterion to assess the convergence of the statistics. We show in Figure 7

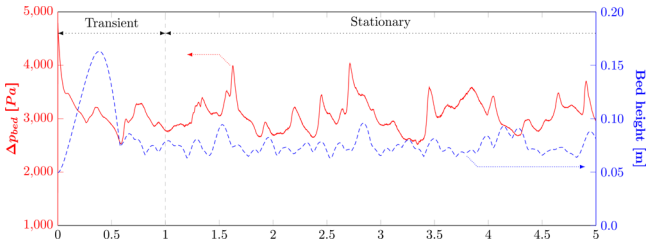

Figure 7. Time evolution of the bed height (dashed blue) and of the dynamic pressure drop across the bubbling bed (solid red).

the typical time evolution of dynamic pressure drop across the bed together with the corresponding time evolution of bed height for a homogeneous bubbling fluidization starting from a bed at rest. All parameters of this simulation are listed in Table 1. The early transient over which the bed expands a lot and the dynamic pressure drop across the bed overshoots is discarded in the analysis. Then, the bed transitions to its stationary (or pseudostationary) bubbling regime, and these two markers oscillate in time around their time-averaged value.

In this stationary regime, we study particles trajectories sampled at a frequency $f_{\text{sample}} = 1/\Delta t_{\text{sample}}$ during a time T_{sample}, and we compute bed statistics. We define a criterion which permits us to determine when statistics converge, i.e., when they remain

Table 1. Parameters of Homogeneous Bubbling Fluidized Bed Considered To Illustrate Bed Statistics Convergence Criterion[a]

parameter	value
particles	
diameter d_p	1 mm
density ρ_p	1500 kg m^{-3}
dimensionless maximum overlapping distance $\delta_{ij,\max}/d_p$	0.05
stiffness coefficient k_n	4000 N m^{-1}
normal restitution coefficient e_n	0.9
Coulomb friction coefficient μ_C	0.4
solid time-step magnitude Δt_p	5×10^{-6} s
fluid	
dimensionless mesh size $\Delta x/d_p$	2
fluid time-step magnitude Δt_f	2×10^{-5} s
density ρ_f	1.2 kg m^{-3}
viscosity μ	1.8×10^{-5} Pa s
fluidization velocity $U_{\text{mf}}(\varepsilon_f = 0.37)$	0.315 m s^{-1}
$U_{\text{in}}/U_{\text{mf}}$	2.5
geometry	
domain size $L_x \times L_y \times L_z$	0.08 m × 0.08 m × 0.2 m
BC on lateral (vertical) boundaries	biperiodic
initial bed height H_0	0.05 m (SCL)
number of particles	80 × 80 × 50 = 320,000
dimensionless numbers	
$\mathcal{R}e_{U_{in}}$	52.53
ρ_p/ρ_f	1500

[a]SCL means Simple Cubic Lattice to describe the initial layout of particles. BC stands for boundary conditions.

the same regardless of T_{sample}. For instance, let us consider the time-averaged sum of all particles velocity norm in the domain. It can be computed in the following way:

$$\langle \text{Sum}|\boldsymbol{v}_p| \rangle_{X,T_{\text{sample}}} = \frac{1}{T_{\text{sample}}} \int_{t_{ss}}^{t_{ss}+T_{\text{sample}}} \sum_{i=0}^{N_p-1} |\boldsymbol{v}_i(t)| dt \approx \frac{1}{N_{T_{\text{sample}}}} \sum_{j=0}^{N_{T_{\text{sample}}}-1} \sum_{i=0}^{N_p-1} 0.5(|\boldsymbol{v}_i(t_j)| + |\boldsymbol{v}_i(t_{j+1})|) \quad (31)$$

where $T_{\text{sample}} = N_{T_{\text{sample}}} \Delta t_{\text{sample}}$, $t_j = t_{ss} + j\Delta t_{\text{sample}}$, $t_0 = t_{ss}$, and $t_{N_{T\text{sample}}} = t_{0,s} + T_{\text{sample}} \cdot t_{ss}$ denotes the starting time of the pseudostationary regime or equivalently the end of the early transient regime (Figure 7, $tss = 1\ s$) . "X" means global statistics, i.e., on all particles or in the whole domain. We consider that the sample duration T_{sample} is large enough to form relevant statistics once $\langle \text{Sum}\,|\boldsymbol{v}_p| \rangle_{X,T_{\text{sample}}}$ reaches a steady value. We therefore introduce the following convergence criterion C:where $\langle \text{Sum}|\widehat{v_p}| \rangle_{X,T_{\text{sample}}}$ and $\langle \text{Sum}|\widetilde{v_p}| \rangle_{X,T_{\text{sample}}}$ represent the maximum and minimum values reached by $\langle \text{Sum}|\boldsymbol{v}_p| \rangle_{X,T_{\text{sample}}}$ over $[t_{ss}, t_{ss}+T_{\text{sample}}]$, and $T_{var.}$ is a time period of variation. The maximum and minimum values of $\langle \text{Sum}|\boldsymbol{v}_p| \rangle_{X,T_{\text{sample}}}$ over $[t_{ss}, t_{ss}+T_{\text{sample}}]$ normalize $C(T_{\text{sample}}, T_{var.})$. The convergence criterion $C(T_{\text{sample}}, T_{var.})$ contains one problem-dependent time parameter $T_{var.}$. To compute $C(T_{\text{sample}}, T_{var.})$, we also assume that Δt_{sample} is a multiple of Δt_f and that $T_{var.}$ is a multiple of Δt_{sample} to avoid any interpolation in time.

DOI: 10.1021/acs.iecr.6b03627

For each flow configuration, we set the values of Δt_{sample} and $T_{var.}$ using characteristic time scales as, e.g., time period of

$$C(T_{\text{sample}}, T_{var}) = \frac{1}{\langle \text{Sum}|\boldsymbol{v}_p| \rangle_{X,T_{\text{sample}}} - \langle \text{Sum}|\boldsymbol{v}_p| \rangle_{X,T_{\text{sample}}}} \cdot \frac{\langle \text{Sum}|\boldsymbol{v}_p| \rangle_{X,T_{\text{sample}}} - \langle \text{Sum}|\boldsymbol{v}_p| \rangle_{X,T_{\text{sample}}-T_{var}}}{T_{var}} \tag{32}$$

pressure drop across the bed oscillations or average convective time scale of particles motion. Figure 8 shows the time

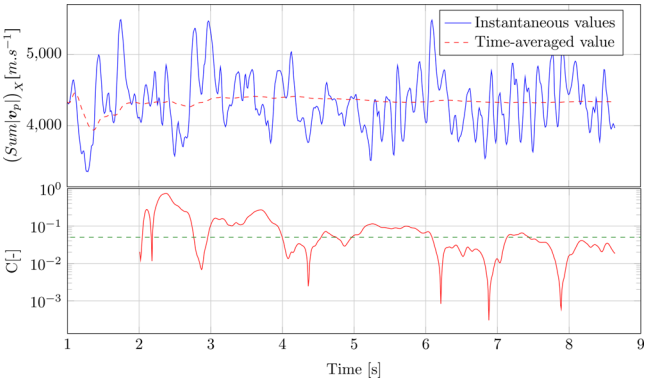

Figure 8. Time evolution of $(\text{Sum}|\boldsymbol{v}_p|)_X$, its time average $\langle \text{Sum}|\boldsymbol{v}_p| \rangle_{X,T_{\text{sample}}}$ (above) and the convergence criterion $C(T_{\text{sample}},T_{var.})$ (below).

evolution of $(\text{Sum}|\boldsymbol{v}_p|)_X$, $\langle \text{Sum}|\boldsymbol{v}_p| \rangle_{X,T_{\text{sample}}}$ and the convergence criterion described above. For that case, we assume that statistics are converged when $C(T_{\text{sample}},T_{var.})$ is less than 0.05 over $T_{var.}$ = 1 s. As shown in Figure 8, this condition is satisfied for Tsample ≃ 7.6 *s*.

3.2. Numerical Parameters. In order to perform simulations as accurate and reproducible as possible, we study the influence of numerical parameters that have a major influence on the computed solution. First, we study the convergence of the numerical method with the solid and fluid time-step magnitudes. Second, as an actual grid size convergence analysis cannot be conducted in relation to the grid size constraint $\Delta V \simeq 10V_p$, we identify what grid size offers the best compromise between accurate resolution of the fluid flow (small grid size) and relevant averaging process (large grid size).

The selected test case is once again a homogeneous bubbling fluidized bed. All simulation parameters are listed in Table 2. The configuration is similar to the one in Section 3.1, but the flow regime is slightly more inertial ($\mathcal{R}e_{U_{\text{in}}}$ = 301.33 versus 52.53 in Section 3.1).

3.2.1. Particle Time Step. In dense fluidized bed simulations performed with our DEM-CFD model, most of the computing time is spent in the Lagrangian tracking of particles with collisions. In his pioneering work on DEM-CFD models, Tsuji[7] emphasized that an accurate resolution of particle−particle and particle−wall contacts is necessary to describe properly the whole fluidized bed dynamics. As usual, we expect our simulation method to be quick and accurate. These two expectations are generally contradictory as far as the time-step magnitude is concerned. In fact, a small time step guarantees accuracy but requires more time steps to be computed for the same physical time and vice versa for a large time step. As in a fluidized bed, the interphase coupling is dominant in the overall dynamics, determining the right compromise between accuracy and fast computing for the solid time-step magnitude Δt_p is not an easy task.

Table 2. Parameters of Homogeneous Bubbling Fluidized Bed Considered to Illustrate the Bed Statistics Convergence Criterion[a]

parameter	value
particles	
diameter d_p	2 mm
density ρ_p	2500 kg m^{-3}
dimensionless maximum overlapping distance $\delta_{ij,\max}/d_p$	0.05
stiffness coefficient k_n	4000 N m^{-1}
normal restitution coefficient e_n	0.9
Coulomb friction coefficient μ_C	0.4
solid time-step magnitude Δt_p	0.25−2 × 10^{-5} s
fluid	
dimensionless mesh size $\Delta x/d_p$	1.47−2.5
fluid time-step magnitude Δt_f	0.5−5 × 10^{-5} s
fensity ρ_f	1.2 kg m^{-3}
viscosity μ	1.8 × 10^{-5} Pa s
fluidization velocity $U_{\text{mf}}(\varepsilon_f = 0.37)$	0.904 m s^{-1}
$U_{\text{in}}/U_{\text{mf}}$	2.5
geometry	
domain size $L_x \times L_y \times L_z$	0.16 m × 0.16 m × 0.5 m
BC on lateral (vertical) boundaries	biperiodic
initial bed height H_0	0.1 m (SCL)
number of particles	80 × 80 × 50 = 320,000
dimensionless numbers	
$\mathcal{R}e_{U_{\text{in}}}$	301.33
ρ_p/ρ_f	2500

[a]SCL means Simple Cubic Lattice to describe the initial layout of particles. BC stands for boundary conditions.

As presented in ref 29, the collision characteristic time *Tcol* arising from the mass-spring-dashpot contact force model used in this work (see Section 2.2) in the case of a normal gravityless collision of two spheres reads as follows:

$$T_{\text{col}} = \frac{\pi}{\sqrt{\omega_0^2 - \gamma_n^2}} \tag{33}$$

with $\omega_0^2 = 2k_n/m_p$. The normal dissipative coefficient γ_n can be related to the coefficient of restitution $e_n \in [0,1]$ in the following way: $\gamma_n = -\frac{\omega_0 \ln e_n}{\sqrt{\pi^2 + (\ln e_n)^2}}$.[29] As contacts are (very often explicitly) integrated in time in soft sphere models, this integration should be carried out at the discrete level with a time step Δt_p much smaller than the contact duration T_{col} to guarantee an accurate resolution of the contact. Practically, it is recommended in the literature[29,40,41] to integrate a dry contact with Δt_p in the range $[T_{\text{col}}/50,\ T_{\text{col}}/15]$. In a fluidized bed, most contacts are physically different from an ideal normal gravityless dry contact, and we hence rely on simulation tests to estimate the appropriate magnitude of Δt_p.

From Table 2 and eq 33, we have T_{col} = 10^{-4} s. We fix $\Delta x/d_p = 2$, $\Delta t_f = 2 \times 10^{-5}$ s and perform a series of simulations with a solid time step Δt_p in the range $[0.25, 2] \times 10^{-5}$ s, i.e., $\Delta t_p \in [T_{\text{col}}/40,\ T_{\text{col}}/5]$. We compare statistics as a function of Δt_p in order to determine the maximal time-step magnitude required in our DEM-CFD simulations to describe accurately the bed dynamics. We plot in Figure 9 the converged statistics of the velocity norm of all particles $\langle \text{Sum}|\boldsymbol{v}_p| \rangle_{X,T_{\text{sample}}}$ as a function of the solid time step Δt_p. Here, $\langle \text{Sum}\ |\boldsymbol{v}_p| \rangle_{X,T_{\text{sample}}}$ converges progressively to a constant value as Δt_p decreases. For $\Delta t_p \leq T_{\text{col}}/10$, the dynamics of the bed seems to be unaffected by the

DOI: 10.1021/acs.iecr.6b03627

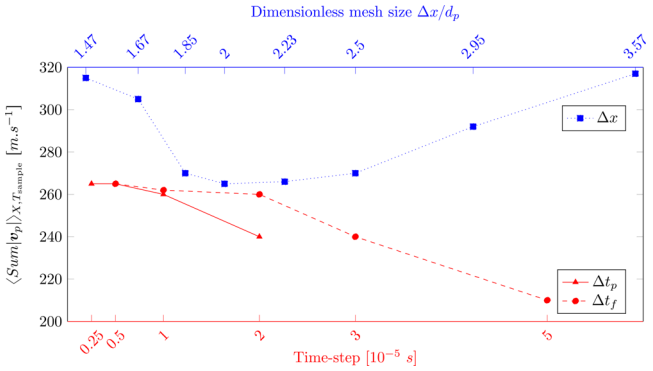

Figure 9. Influence of solid time-step magnitude (red line), fluid time-step magnitude (red dotted line), and fluid grid size (blue dotted line) on the time-averaged sum of all particles velocity norm, selected as a major feature of the computed solution.

magnitude of Δt_p. Interestingly, this upper bound for Δt_p is higher that the one generally used for dry granular simulations performed with the same DEM code that generally around $T_{col}/20$.[29] Actually, in a fluidized bed, particles motion is as much driven by the hydrodynamic force $\boldsymbol{f}_{fp}$ than the collision force $\boldsymbol{f}_{pp}$. For high U_{in}/U_{mf} ratios, $\boldsymbol{f}_{fp}$ actually dominates $\boldsymbol{f}_{pp}$. This sheds some light on why the dry granular upper bound is not directly applicable to DEM-CFD simulations.

Another constraint on the solid time-step magnitude Δt_p common to dry granular simulations and DEM-CFD simulations is related to the maximum displacement of each individual particle over Δt_p with respect to the maximum overlap distance per particle allowed over a contact $\delta_{ij,max}$ (also referred to in DEM models as crust thickness[29]). Indeed, in a soft sphere model, a particle should not move more than its crust thickness over Δt_p, otherwise two colliding particles may overlap more than allowed to. This condition reads as follows:

$$\mathrm{CFL}_{\mathrm{particle}} = \frac{\mathbf{v}_{ij}\Delta t_p}{\delta_{ij,\max}} < 1 \tag{34}$$

where $\boldsymbol{v}_{ij}$ is the relative velocity between colliding particles i and j. It is somehow similar to a Courant–Friedrichs–Lewy (CFL) stability condition for the fluid motion. The crust thickness $\delta_{ij,max}$ is a fixed simulation parameter, set in our simulations to $\delta_{ij,max}/d_p = 0.05$ (Table 2). An upper bound for $\boldsymbol{v}_{ij}$ needs to be estimated before the simulation in order to properly set Δt_p according to relation 34. Note that our DEM solver uses a constant time-step integration and is not able to perform local time-step adaption. In practice, as the estimation of the upper bound for $\boldsymbol{v}_{ij}$ is not straightforward, we introduce a safety coefficient of 2 and require the following condition $\mathrm{CFL}_{\mathrm{particle}} < 0.5$ to be satisfied.

In the case of homogeneous bubbling fluidized beds with an inlet velocity U_{in} ranging from U_{mf} to $7U_{mf}$, extensive computing indicates that the following empirical formula:

$$\widehat{|\mathbf{v}_p|} = 2U_{\mathrm{in}}\ln\left(\frac{U_{\mathrm{in}}}{U_{\mathrm{mf}}}\right) \tag{35}$$

is a reliable approximation of the maximum particle velocity norm (in the sense over all particles and a long enough simulation time). Thus, the solid time step Δt_p in homogeneous bubbling fluidized bed simulations is set as a combination of the $\mathrm{CFL}_{\mathrm{particle}}$ condition and the contact integration condition as follows:

$$\Delta t_p = \min\left(\frac{T_{\mathrm{col}}}{10}, \frac{0.5\delta_{ij,\max}}{\widehat{|\mathbf{v}_p|}}\right) \tag{36}$$

3.2.2. Fluid Time Step. The explicit treatment of the advective term in the fluid momentum eq 4 requires the fluid time step Δt_f to satisfy a CFL condition to ensure stability. For constant grid size Δx in all 3 directions, the CFL condition reads as follows:

$$\mathrm{CFL} = \max_{d=1,2,3}\ \max_{j}\ \frac{|u_{f,d,j}|\Delta t_f}{\Delta x} < \mathrm{CFL}_{\max} \tag{37}$$

where d denotes the space direction index, j the velocity node index, and $u_{f,d,j}$ the d component of $\boldsymbol{u}_f$ at velocity node j. For our first-order explicit treatment of the advection term, CFL_{max} is theoretically 1. In practice, we use a safety coefficient of 2 and impose CFL < 0.5 instead. As for the granular time-step magnitude Δt_p, we do not known a priori what will be the value of $\max_{d=1,2,3}\ \max_j\ |u_{f,d,j}|$ over a whole simulation. Extensive computing indicates that high solid volume fraction heterogeneities lead to local velocity overshoots as large as 10 times the inlet velocity. Then, a first constraint to determine the magnitude of Δt_f is as follows:

$$\Delta t_f < \frac{0.5\Delta x}{10U_{\mathrm{in}}} \tag{38}$$

However, contrary to the granular flow solver, the fluid solver possesses a local time adaption mechanism to ensure stability by temporarily splitting the diffusion–advection problem (eq 4) into a separate diffusion subproblem and a separate advection subproblem and subtime stepping the advection subproblem such that eq 37 is recovered. The advection subproblem is hence solved m consecutive times with a time step Δt_{adv} as follows:

$$\rho_f\frac{\mathcal{E}_f^n\tilde{u}_f^{n+(k+1)/m} - \mathcal{E}_f^{n-1}\tilde{u}_f^{n+k/m}}{\Delta t_{\mathrm{adv}}} = -\rho_f\nabla\cdot(\mathcal{E}_f^{n-1}\tilde{u}_f^{n+k/m}\tilde{u}_f^{n+k/m}), \quad k = 0, \ldots, m-1 \tag{39}$$

with Δt_{adv} satisfying (37), $m \times \Delta t_{adv} = \Delta t_f$, $\tilde{\boldsymbol{u}}_f^n = \boldsymbol{u}_f^n$ and $\boldsymbol{u}_f^* = \tilde{\boldsymbol{u}}_f^{n+1}$. It is recommended not to perform these subiterations too often over a simulation as it affects the time accuracy of the solution. If this does happen too often, it is safer to redo the simulation with a smaller Δt_f.

The second constraint to determine Δt_f derives from the loose (explicit) coupling of the fluid and solid governing equations in our solution algorithm. In fact, we solve the fluid governing equations for a fixed position and reaction source term of the particles computed at the previous time and then advance the particles for a fixed hydrodynamic force exerted on them. In other words, the particles as seen by the fluid are frozen over Δt_f and similarly the fluid as seen by the particles is frozen over Δt_f. If Δt_f is "small enough", this loose coupling strategy yields a reasonably accurate time evolution of the system. However, to the best of our knowledge, there is no theoretical way to estimate an upper bound of Δt_f that enables one to avoid a nonphysical and nonrealistic evolution of the system. Hence, we rely once again on extensive computing to empirically determine the optimal magnitude of Δt_f. We fix $\Delta x/d_p = 2$, $\Delta t_p = T_{col}/20 = 5 \times 10^{-6}$ s and perform a series of simulations with a fluid time step Δt_f in the range $[T_{col}/20, T_{col}/2]$. In all these simulations, Δt_f satisfies eq 37. We compute

DOI: 10.1021/acs.iecr.6b03627

the statistics of the bed as a function of Δt_f. In Figure 9, we plot as a dashed red line the velocity norm of all particles $\langle \mathrm{Sum}|\boldsymbol{v}_p|\rangle_{X,T_{\mathrm{sample}}}$ versus Δt_f. For $\Delta t_f < T_{\mathrm{col}}/5$, $\langle \mathrm{Sum}|\boldsymbol{v}_p|\rangle_{X,T_{\mathrm{sample}}}$ is almost independent of Δt_f, giving an upper bound for describing properly the bed dynamics. Since the solution of the fluid problem is rather computationally inexpensive with respect to the Lagrangian tracking of particles with collisions, a sensible guideline seems to be $\Delta t_f \leq T_{col}/5$. This guideline has proven to be reliable in our simulations. Note that the loose coupling of the fluid and solid governing equations can be improved in different ways as, e.g., (i) using a second order time accurate leapfrog algorithm for the fluid solver in the same spirit as the granular solver or (ii) interpolating the fluid velocity field at particles positions both in time and in space as particles move and hence update $\boldsymbol{f}_{pp}$ at each granular solver subtime. Improvement (ii) will increase considerably the computing cost but should enable us to compute solutions of higher precision and stability. This is a topic of ongoing work for the enhancement of our DEM-CFD model.

3.2.3. Fluid Grid Size. Our DEM-CFD numerical model is based on a unique grid to solve the Navier−Stokes equations, to compute $\mathcal{E}_f$ and to compute the fluid−solid interphase coupling. In other words, contrary to, e.g., ref 6, our projection operator from Lagrangian to Eulerian depends on the grid size Δx. A true grid size convergence analysis cannot be performed as Δx must satisfy (30) or at least $V_p < \Delta x^3$ to avoid $\mathcal{E}_f = 0$ (Section 2.5). In any case, Δx cannot tend to zero as in a classical grid size convergence analysis. What we can however investigate in the range $\Delta x \in [1.47\ d_p; +\infty]$ is the lower and upper bounds of Δx to guarantee quasi-grid independent computed results. Once again, the method requires a large enough Δx for the spatial averaging process and a small enough Δx to properly capture the fluid flow dynamics. To estimate the optimal grid size range, we fix $\Delta t_p = T_{\mathrm{col}}/20 = 5 \times 10^{-6}$ s, $\Delta t_f = 10^{-5}$ s $= 2\Delta t_p$ and perform a series of simulations with $\Delta x \in [1.47\ d_p, 3.57\ d_p]$. We plot $\langle \mathrm{Sum}|\boldsymbol{v}_p|\rangle_{X,T_{\mathrm{sample}}}$ versus Δx in Figure 9 as a representative measure of bed statistics. It is pretty visible that bed statistics are quasi independent of Δx for $\Delta x \in [1.85\ d_p, 2.5\ d_p]$. The trend is similar for other measures of bed statistics. The lower bound is in agreement with the theoretical lower bound (eq 27) for the separation of scales (1 order of magnitude) as originally introduced by.[42] All simulations in the rest of the paper are performed with Δx close to 2 d_p.

3.3. Domain Size Influence. In fluidized beds, large flow structures such as particles clustering, i.e., regions of low $\mathcal{E}_f$, and fluid bubbles, i.e., regions of high $\mathcal{E}_f$ (close to 1), develop in the core of the bed. The size of these structures is controlled by the flow regime, i.e., the dimensionless numbers that govern the system (density ratio, Reynolds number, $U_{\mathrm{in}}/U_{\mathrm{mf}}$ ratio), and the lateral boundary conditions. Although it is known (and rather intuitive) that the domain size controls the dynamics of the system with lateral solid wall boundary conditions (no slip condition on the fluid velocity), biperiodic domains are assumed to represent infinitely large domains in directions of periodicity. However, the size of the computational domain in each periodic direction needs to be larger than the characteristic length scale of the system dynamics for this assumption to hold. If this assumption is not satisfied, the size of these representative flow structures (essentially fluid bubbles) can match the domain size, and then, a bubbling bed can degenerate into a slugging bed as presented in Figure 10, even with biperiodic boundary conditions. In fact, if the domain is transversely (horizontally) too narrow and a particles cluster is as large as the domain cross section, the fluid cannot easily flow through this cluster. Instead, a fluid bubble manifests upstream of the particles cluster, grows, and carries upward the cluster as an homogeneous dense pack of particles, as shown in Figure 10b.

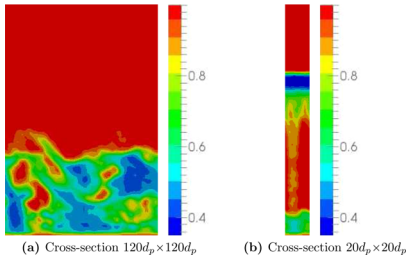

Figure 10. Snapshots at t = 2.8 s of the fluid volume fraction spatial distribution in a homogeneous bubbling fluidized bed in a vertical cut plane for domains with (a) a wide cross section and (b) a narrow cross section.

Particles progressively plummet downward from the bottom of the cluster to the bottom of the bed until the cluster vanishes and another cluster (slug) appears. This cyclic slugging behavior is representative of narrow fluidized beds. In fact, the primary instability, i.e., the vertical instability, can develop while the secondary transverse instability is damped by the narrowness of the domain. Conversely, with all other parameters kept the same, if the domain cross section is large enough, in the sense larger than the largest particles cluster, the fluid flows across these clusters more easily, and the secondary transverse instability develops. As shown in Figure 10a, the size of created bubbles is not controlled by the domain cross section, and the bed dynamics is totally different.

From these preliminary results, it is rather remarkable that the bed dynamics is strongly affected by the computational domain periodic size. A valuable question to answer is the minimum domain size for a certain flow regime to exhibit cross-section size-independent bed statictics and behavior, such that the biperiodic simulation indeed represent an infinitely larger fluidized bed. Performing computations in a small biperiodic domain is tempting as it involves less computing resources but at the cost of producing physical results biased by the domain cross-section size.

To highlight the influence of the cross-section size of biperiodic domains, we perform a series of simulations in domains of increasing cross-section size and examine how this affects bed statistics, in the same manner as in ref 6. This survey is carried out with three-dimensional systems as two- and three-dimensional beds do not lead to the same statistics and presumably to different dynamics. The initial configuration is a simple cubic arrangement of 50 particles height, and the number of particles and the domain size in the transverse directions are increased simultaneously. Simulations are performed on domains with a cross section in the range of $20d_p \times 20d_p$ to $120d_p \times 120d_p$. All other parameters are similar to the ones used in Section 3.1 and listed in Table 1. Converged in time bed statistics are plotted in Figure 11. The top row shows axial profiles of time-averaged porosity $\langle \mathcal{E}_f \rangle_{T_{\mathrm{sample}}}$ and time-averaged particles velocity norm $\langle \mathrm{Sum}|\boldsymbol{v}_p|\rangle_{T_{\mathrm{sample}}}$ and the bottom row their corresponding time variance. Please note that $\langle \mathrm{Sum}|\boldsymbol{v}_p|\rangle_{T_{\mathrm{sample}}}$ is

DOI: 10.1021/acs.iecr.6b03627

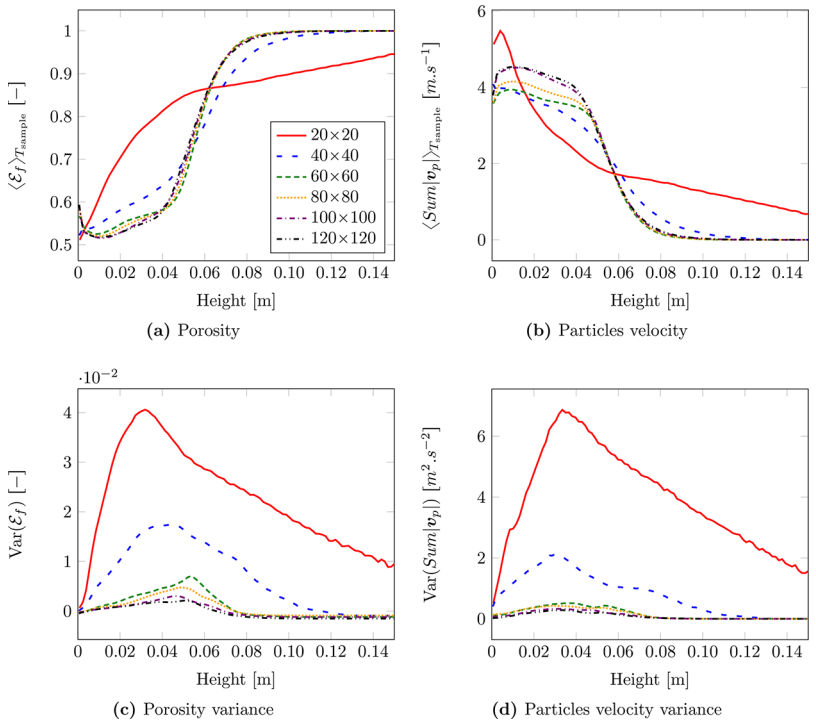

(a) Porosity (b) Particles velocity

(c) Porosity variance (d) Particles velocity variance

Figure 11. Axial profile of bed statistics for domains of increasing cross section.

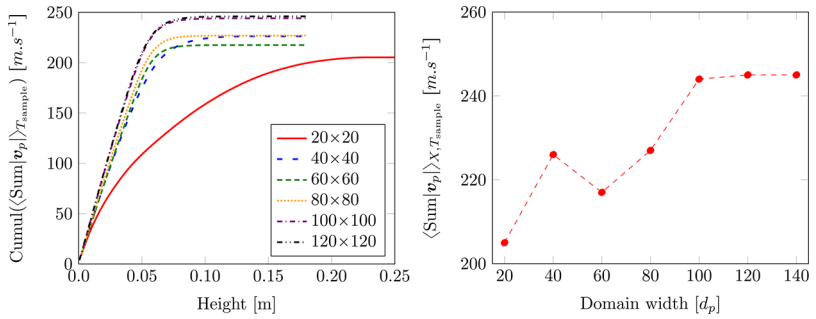

Figure 12. Influence of the domain cross-section size on the time-averaged particles velocity norm.

divided by the cross-section area such that results can be properly compared to each other. Results for the smallest domain $20d_p \times 20d_p$ markedly depart from other cases. The time-averaged porosity axial profile shows a significantly higher (respectively lower) presence of particles in the low (respectively high) region of the bed. This more homogeneous distribution of particles is related to the slugging regime, i.e., the cyclic rise of large fluid bubbles that occupy the whole domain cross section. Besides, $\langle \mathcal{E}_f \rangle_{T_{\text{sample}}}$ reaches 1 at a much higher vertical coordinate, indicating that the time averaged bed height for the domain with a $20d_p \times 20d_p$ cross section is larger than that of domains with a larger cross section. From the domain with a $40d_p \times 40d_p$ cross section, the bed qualitatively behaves in the same way but bed statictics are unaffected by the domain cross-section size from $100d_p \times 100d_p$ only. In Figure 11, we plot the axial profile of the time-averaged cumulative particles velocity norm divided by the cross-section area, while Figure 12 shows the time-averaged velocity norm of all particles (note that as expected the cumulative particles velocity norm at the top of the bed matches the velocity norm of all particles). Once again, these two figures confirm that for domains with a cross section larger than $100d_p \times 100d_p$, the bed behavior is unchanged.

For the particular case studied here, the minimum domain cross-section size to yield cross-section independent results is $100d_p \times 100d_p$. It also signifies that performing computations with a domain cross section larger than $100d_p \times 100d_p$ would not bring any additional knowledge of the system but will essentially require unnecessarily larger computing resources. The result $100d_p \times 100d_p$ as a minimal domain cross section can unfortunately not be generalized to other flow configurations as the minimal domain cross section depends on the flow regime and presumably on the initial bed height to cross-section length ratio. Our objective here is primarily to point out that the assumption that periodic or biperiodic fluidized beds mimic infinitely large fluidized beds strongly depends on the geometric configuration and dimensionless parameters and has to be very meticulously investigated, either with reliable theoretical arguments or by numerical experimentation.

4. VALIDATION AGAINST PHYSICAL DATA

We select two configurations: (i) a homogeneous bubbling fluidized bed for which we compare our numerical predictions to theoretical results and (ii) a spouted bed for which we compare our numerical predictions to experimental data.

DOI: 10.1021/acs.iecr.6b03627

4.1. Onset of Fluidization in a Bubbling Fluidized Bed.

This first validation test corresponds to a homogeneous bubbling fluidized bed with solid wall boundary conditions on the vertical walls. The homogeneous (in the sense constant in space over the bottom wall) inlet velocity U_{in} is increased step by step until the particles begin to bubble and is then reduced back to zero. At each step, the simulation is run until a new pseudostationary state is reached. This test case is basic but very valuable to verify both the minimum fluidization velocity U_{mf} and the dynamic pressure drop across the bed Δp_{bed}. When the bed is fluidized, Δp_{bed} is equal to the total net weight of the bed of particles W_{bed}. The prediction of U_{mf} is obtained by solving the balance equation between Δp_{bed} as predicted by Ergun's equation and W_{bed} as follows:

$$150\frac{(1-\mathcal{E}_{f,mf})^2}{\mathcal{E}_{f,mf}^3}\frac{\mu_f U_{mf}}{d_p^2} + 1.75\frac{(1-\mathcal{E}_{f,mf})}{\mathcal{E}_{f,mf}^3}\frac{\rho_f U_{mf}^2}{d_p} = (1-\mathcal{E}_{f,mf})(\rho_p-\rho_f)g \quad (40)$$

where $\mathcal{E}_{f,mf}$ denotes the porosity of the bed at the onset of fluidization. Another interesting and documented phenomenon is the expected hysteresis of the dynamic pressure drop across the bed between increasing and decreasing the inlet velocity U_{in} (see, e.g., ref 43). The complete set of parameters for this system is given in Table 3.

Table 3. Parameters of Fluidized Bed Considered for Validation Test $\Delta p = f(U_{in})$[a]

parameter	value
particles	
diameter d_p	2 mm
density ρ_p	1500 kg m^{-3}
dimensionless maximum overlapping distance $\delta_{ij,max}/d_p$	0.05
stiffness coefficient k_n	4000 N ·m^{-1}
normal restitution coefficient e_n	0.9
Coulomb friction coefficient μ_C	0.4
solid time-step magnitude Δt_p	2 × 10^{-5} s
fluid	
dimensionless mesh size $\Delta x/d_p$	2
fluid time-step magnitude Δt_f	4 × 10^{-5} s
density ρ_f	1.2 kg m^{-3}
viscosity μ	1.8 × 10^{-5} Pa s
fluidization velocity $U_{mf}(\varepsilon_f = 0.378)$	0.692 m s^{-1}
U_{in}/U_{mf}	0−1.3
geometry	
domain size $L_x \times L_y \times L_z$	0.08 m × 0.08 m × 0.6 m
BC on lateral (vertical) boundaries	walls
initial bed height H_0	≈0.335 m
number of particles	320,000
dimensionless numbers	
$\mathcal{R}e_{U_{mf}}$	93.33
ρ_p/ρ_f	1500

[a]BC stands for boundary conditions.

The initial layout of particles in the domain is the results of a purely granular simulation (without fluid) in which particles are inserted at the top of the domain, settle under gravity, and collide and arrange themselves at the bottom of the domain. The initial bed height H_0 exhibits a porosity of $\mathcal{E}_{f,0} \approx 0.378$, relevant of the empirical value of random close packing. As we increase the inlet velocity U_{in}, Δp_{bed} rises from zero and follows the Ergun equation with $\mathcal{E}_f = \mathcal{E}_{f,0}$ until an inlet velocity threshold slightly above $U_{mf}(\mathcal{E}_{f,0})$ is reached. At that stage, particles begin to vibrate and rearrange themselves while the dynamic pressure drop across the bed slightly decreases and stabilizes at $\Delta p_{bed} = W_{bed}$. This moderate pressure drop overshoot arises from a specific arrangement of particles in the presence of walls for systems whose particle−reactor size ratio does not satisfy the condition $d_p/Lx \ll 1$.[43] Here, this ratio is 0.025 and is apparently not small enough to prevent the appearance of this hysteresis phenomenon. The physical comprehension of this hysteresis phenomenon is well established. Granular arches form in the random pack of particles and these structures cause higher flow resistance than if particles were free to move.[43] While decreasing the inlet velocity from $U_{in} > U_{mf}$ to $U_{in} = 0$, particles begin to settle for a higher velocity than the one they started to vibrate from while increasing U_{in}. They hence arrange themselves in such a way that flow resistance is minimized. In the case presented in Figure 13, this arrangement corresponds to a

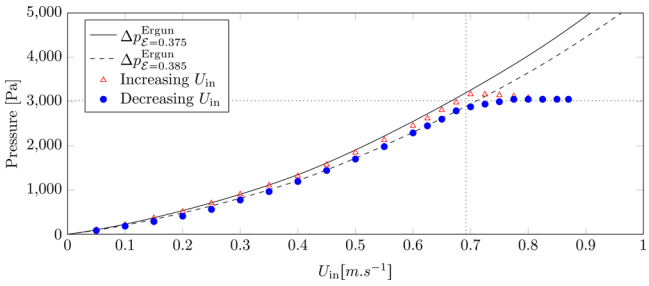

Figure 13. Dynamic pressure drop across the bed as a function of the inlet flow velocity.

bed porosity of $\mathcal{E}_{f,mf} = 0.385$. Assuming $\mathcal{E}_{f,mf} \simeq \mathcal{E}_{f,0} = 0.378$ and $H_{mf} \simeq H_0$ and (40), the theoretical dynamic pressure drop across the bed once the bed is fluidized is $\Delta p_{fluidizedbed} = (1-\mathcal{E}_{f,0})(\rho_p-\rho_f)gH_0 \approx 3017$Pa. The value computed by our model is ≈3050Pa, in very satisfactory agreement with the theoretical estimate.

Our model reproduces well the main features of the selected fluidized bed. In fact, dynamic pressure drop across the bed and minimum fluidization velocity are both satisfactorily predicted. The expected hysteresis phenomenon is also qualitatively well reproduced by the model. This simple but essential validation case gives confidence in the consistency of our set of governing equations as well as in the numerical implementation of the model.

4.2. Dynamics of Spouted Beds.

Experimental data available for 3D bubbling beds are generally limited to macroscopic measures as average bed height, pressure drop across the bed or minimum fluidization velocity as experimental measurements in the core of the bed remains challenging. Quasi-3D or 2.5D configurations (i.e., one dimension of the cross section only spans a few particle diameters) enable one to better visualize the bed dynamics and its corresponding flow structures. These configurations hence yield more precise data in the core of the bed to compare our DEM-CFD numerical model's predictions to. The second validation case is hence a quasi-3D spouted bed for which experimental data are available.

We compare our numerical results to experimental data collected by Brown over his Ph.D thesis.[44] The spouted bed

DOI: 10.1021/acs.iecr.6b03627

configuration is presented in Figure 14. Lateral (vertical) boundaries are solid walls. Glass particles with two different diameters

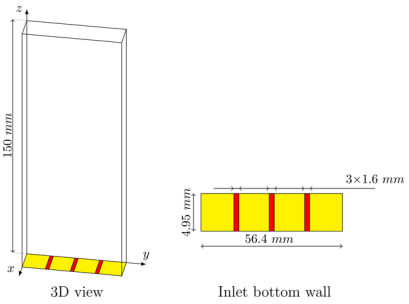

Figure 14. Domain geometry of the spouted bed experiment used by Brown.[44]

d_p = 550 μm and d_p = 750 μm and three different injection conditions, namely, single, double, or triple nozzles, were investigated in the experiments. All parameters for the d_p = 550 μm and d_p = 750 μm systems are listed in Tables 4 and 5,

Table 4. Parameters of Spouted Fluidized Bed of Brown[44] with Particles of Diameter d_p = 550 μm[a]

parameter	value
particles	
diameter d_p	0.550 mm
density ρ_p	2500 kg m^{-3}
dimensionless maximum overlapping distance $\delta_{ij,\max}/d_p$	0.05
stiffness coefficient k_n	10000 N m^{-1}
normal restitution coefficient e_n	0.9
Coulomb friction coefficient μ_C	0.1
solid time-step magnitude Δt_p	1 × 10^{-6} s
fluid	
dimensionless mesh size $\Delta x/d_p$	
in x direction	2.927
in y direction	3
in z direction	1.818
fluid time-step magnitude Δt_f	5 × 10^{-6} s
density ρ_f	1.2 kg m^{-3}
viscosity μ	1.8 × 10^{-5} Pa s
fluidization velocity $U_{mf}(\varepsilon_f = 0.395)$	0.24 m s^{-1}
U_{bulk}/U_{mf}	3 (except for Figure 17, 2.6)
geometry	
domain size $L_x \times L_y \times L_z$	0.0564 m × 0.00495 m × 0.15 m
BC on lateral (vertical) boundaries	walls
initial bed height H_0	0.052 m
number of particles	100,000
dimensionless numbers	
$\mathcal{R}e_{U_{bulk}}$	26.4
$\mathcal{R}e_{U_{in,1N}}$	930.6
ρ_p/ρ_f	2500

[a]BC and 1N stand for boundary conditions and one nozzle, respectively.

respectively. The bulk velocity U_{bulk} is defined as the mean velocity over the whole bed horizontal cross section and is related to the inlet velocity U_{in} by the following simple formula:

$$U_{bulk} = \frac{1.6 N_{nozzles}}{56.4} U_{in} \quad (41)$$

Table 5. Parameters of Spouted Fluidized Bed of Brown[44] with Particles of Diameter d_p = 750 μm[a]

parameter	value
particles	
diameter d_p	0.750 mm
density ρ_p	2500 kg m^{-3}
dimensionless maximum overlapping distance $\delta_{ij,\max}/d_p$	0.05
stiffness coefficient k_n	10000 N m^{-1}
normal restitution coefficient e_n	0.9
Coulomb friction coefficient μ_C	0.1
solid time-step magnitude Δt_p	1.5 × 10^{-6} s
fluid	
dimensionless mesh size $\Delta x/d_p$	
in x direction	2.927
in y direction	3
in z direction	1.818
fluid time step-magnitude Δt_f	4.5 × 10^{-6} s
density ρ_f	1.2 kg m^{-3}
viscosity μ	1.8 × 10^{-5} Pa s
fluidization velocity $U_{mf}(\varepsilon_f = 0.41)$	0.43 m s^{-1}
U_{bulk}/U_{mf}	3
geometry	
domain size $L_x \times L_y \times L_z$	0.0564 m × 0.00495 m × 0.15 m
BC on lateral (vertical) boundaries	walls
initial bed height H_0	0.07 m
number of particles	50,000
dimensionless numbers	
$\mathcal{R}e_{U_{bulk}}$	64.5
$\mathcal{R}e_{U_{in,1N}}$	2273.6
ρ_p/ρ_f	2500

[a]BC and 1N stand for boundary conditions and one nozzle, respectively.

where 56.4 is the bed width, 1.6 the width of each individual nozzle slit (Figure 14) and $N_{nozzles} \in \{1,2,3\}$ is the number of nozzles. As $N_{nozzles}$ increases, U_{in} is divided by $N_{nozzles}$ such that U_{bulk} is constant regardless of $N_{nozzles}$.

Figures 15 and 16 show the time-averaged fluid volume fraction distribution $\langle \mathcal{E}_f \rangle_{T_{sample}}$ in an x–z plan for the three injection conditions and for the two particle diameters, d_p = 550 μm and d_p = 750 μm, respectively. Both bed height and particles spatial distribution are faithfully reproduced by our model. The agreement is particularly satisfactory for the double- and triple-nozzle cases and slightly less for the single-nozzle cases. In ref 45, the authors, who also compared their numerical predictions with the same grid size to Brown's experiments, attributed the observable discrepancies between numerical results and experimental data to the coarse fluid grid size. In fact, in both the simulations of[45] and ours, the channel width is discretized by a single fluid cell. However, the grid size employed for the single-nozzle cases is the same as the one for the double- and triple-nozzle cases. It seems to us that the argument of low fluid flow resolution might not be the only explanation. It is however expected that a DEM-CFD model as the one of ref 6 that permits us to use a smaller grid size would improve the quality of the computed results and would presumably match more accurately experimental data. Another plausible explanation is that single-nozzle experiments led to a higher level of experimental uncertainty or were more difficult to time average. Nevertheless, computed pressure fluctuations at the inlet cross section of the

DOI: 10.1021/acs.iecr.6b03627

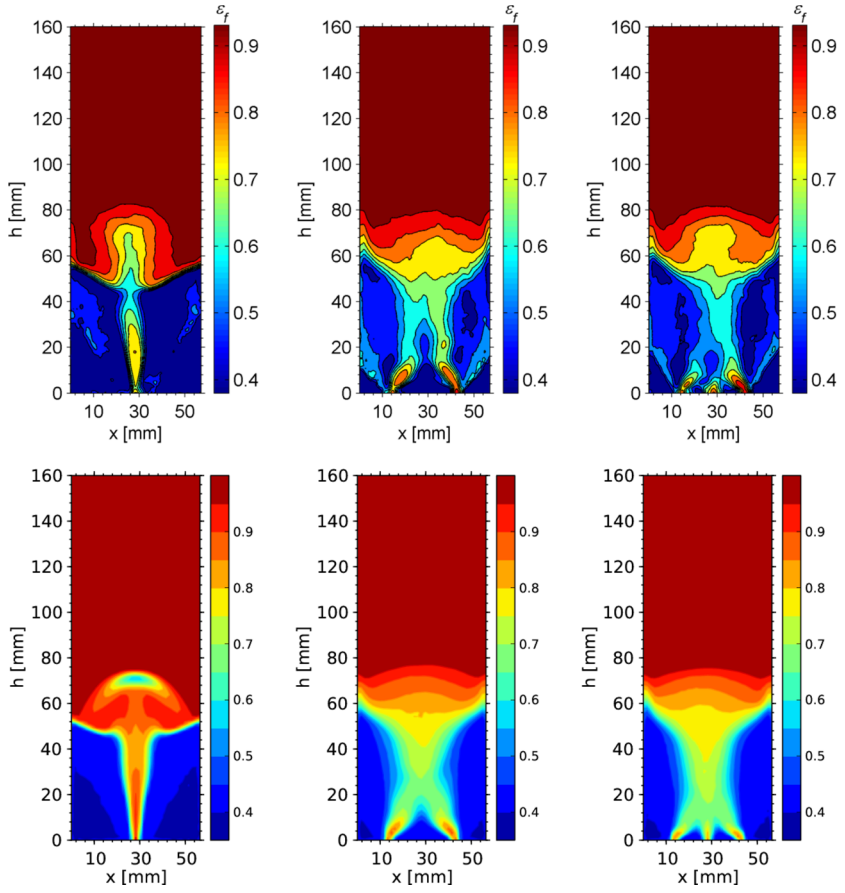

Figure 15. Time-averaged fluid volume fraction contour plots for 1, 2, and nozzles (left to right), U_{bulk}/U_{mf} = 3 and d_p = 550 μm. Top: Brown's experiments.[44] Bottom: Our simulation results. Top figures reprinted in part with permission from Brown, S. L., *Hydrodynamics and Transient Heat Transfer Characteristics in Fluidized and Spouted Beds*. M.Sc. Thesis, Virginia Polytechnic Institute and State University.[44] Copyright 2012, Steven L. Brown.

domain for the single-nozzle case with d_p = 550 μm and U_{bulk}/U_{mf} = 2.6 is close those measured by Brown as shown in Figure 17. The satisfactory agreement of the pressure fluctuations spectrum emphasizes that the bubbles creation and migration dynamics is very well predicted by our model. In this case, the fact that the spectrum shows a single well-defined frequency peak indicates that the dynamics of the system is very cyclic: every 1/10 = 0.1 s, a bubble forms downstream of the nozzle, rises, and bursts at the free surface.

5. INFLUENCE OF THE FRICTION COEFFICIENT ON THE DYNAMICS OF A SPOUTED BED

In a spouted bed, the relative collisional velocity between particles carried upward by the channel flow and particles at the channel flow/lateral static regions interface is generally pretty high. These contacts are mostly tangent. Hence, the relative magnitude of the tangential friction force to the hydrodynamic force exerted by the fluid influences the bed dynamics. In our contact model, the tangential friction force magnitude is controlled by a single material parameter: the Coulomb friction coefficient μ_C. The value of this coefficient is itself strongly dependent on particle surface roughness that can significantly evolve over time due to mutiple successive collisions. As an example, glass beads have a friction coefficient ranging from μ_C = 0.05 for highly polished surfaces to μ_C = 0.7 for rough surfaces. Hence, a particle that experiences numerous high speed collisions may see its surface wearing down over time and the corresponding μ_C markedly increasing. In a spouted bed, particles with a high μ_C will resist more to the entrainment of the fluid in the central channel. This results in a different bed behavior. Our objective here is to capture this effect quantitatively on the single-nozzle configuration with d_p = 750 μm examined in Section 4.2.

The overall dynamics of a single-nozzle spouted bed is as follows. Particles right above the injection nozzle experience a large hydrodynamic force due to the high injection velocity. Their momentum is transferred to the surrounding static particles through normal and tangential contact forces. These static particles are then pushed aside and upward, leading to the creation of a fluid bubble. The fluid bubble grows in size and starts to rise through the bed, fed by continuous fluid injection. As the fluid manages to flow with less resistance through the bed, the pressure drop across the bed decays. The higher granular pressure in the quasi-static dense regions on the sides of the central channel flow pushes particles back into the fluid bubble. While the bubble rises, some particles from the quasi-static dense regions start to fill the fluid region above the nozzle. The fluid flow experiences again a strong resistance and the pressure drop across the bed increases. While a first bubble reaches the bed surface and bursts, a new bubble is created above the injection nozzle and moving particles are trapped between the two bubbles. These moving particles, that move at a high velocity, collide with particles in the quasi-static dense regions on the sides of the channel. In general, as fluid bubbles

DOI: 10.1021/acs.iecr.6b03627

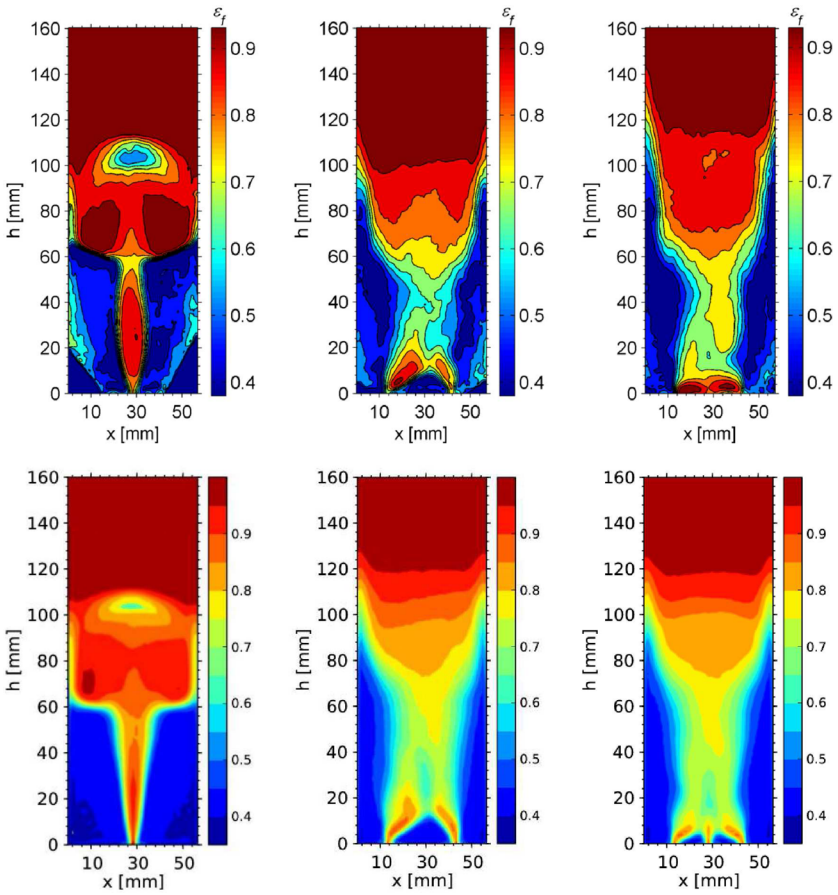

Figure 16. Time-averaged fluid volume fraction contour plots for 1, 2, and nozzles (left to right), U_{bulk}/U_{mf} = 3 and d_p = 750 μm. Top: Brown's experiments.[44] Bottom: Our simulation results. Top figures reprinted in part with permission from Brown, S. L., *Hydrodynamics and Transient Heat Transfer Characteristics in Fluidized and Spouted Beds*. M.Sc. Thesis, Virginia Polytechnic Institute and State University.[44] Copyright 2012, Steven L. Brown.

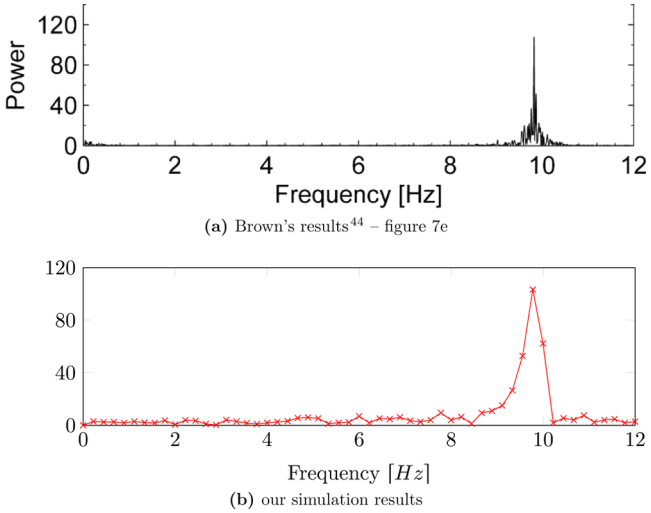

(a) Brown's results[44] – figure 7e

(b) our simulation results

Figure 17. Frequency spectrum of the dynamic pressure oscillations at the inlet cross section for the single-nozzle case, U_{bulk}/U_{mf} = 2.6 and d_p = 550 μm. Top: Brown's experiments.[44] Bottom: Our simulation results. Top figure reprinted in part with permission from Brown, S. L., *Hydrodynamics and Transient Heat Transfer Characteristics in Fluidized and Spouted Beds*. M.Sc. Thesis, Virginia Polytechnic Institute and State University.[44] Copyright 2012, Steven L. Brown.

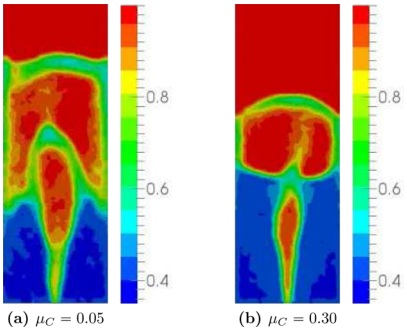

(a) μ_C = 0.05 (b) μ_C = 0.30

Figure 18. Snapshots at t = 1.5 s of the fluid volume fraction spatial distribution for two different values of the tangential friction coefficient μ_C = 0.05 and μ_C = 0.3 in the single-nozzle spouted bed.

rise with a high velocity, they propel entrained particles above the bed height. As particles disperse above the bed height and experience a lower upward hydrodynamic force, they plummet on both sides of the channel.

On the basis of the above, it is rather predictable that the magnitude of μ_C quantitatively modifies the bed dynamics. For low values of μ_C, fluid bubbles are larger than for high μ_C and generally wider than the injection nozzle. This effect is related to the lower tangential resistance to displacement experienced by particles set in motion by rising bubbles. This also impacts the migration of fluid bubbles to the bed surface that rise faster than for high μ_C. As a result, particles trapped between two bubbles are propelled higher (Figure 18) and settle laterally

DOI: 10.1021/acs.iecr.6b03627

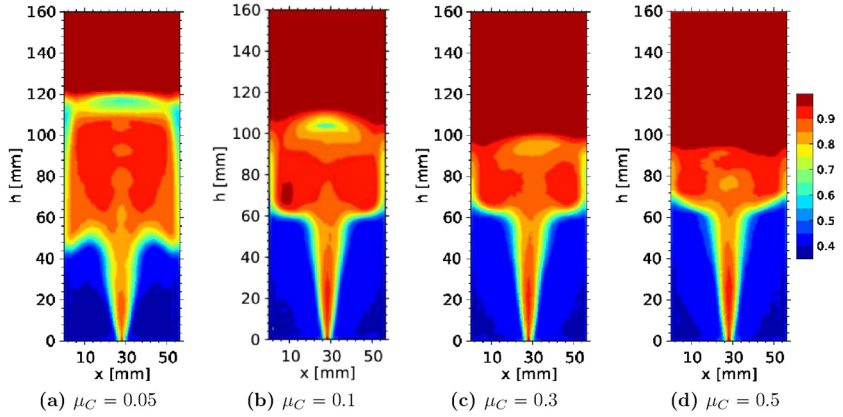

(a) $\mu_C = 0.05$ (b) $\mu_C = 0.1$ (c) $\mu_C = 0.3$ (d) $\mu_C = 0.5$

Figure 19. Time-averaged fluid volume fraction contour plots for different values of the tangential friction coefficient μ_C in the single-nozzle spouted bed.

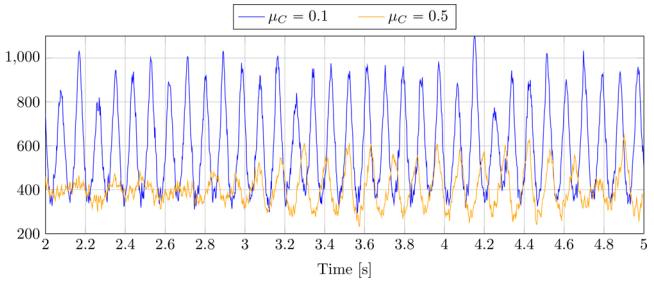

Figure 20. Time evolution of the dynamic pressure drop across the bed for two different friction coefficients μ_C = 0.1 and μ_C = 0.5 in the single-nozzle spouted bed.

farther from the central channel (i.e., closer to the walls), in a fountain-like shape (Figure 19a). Finally, as a new bubble detaches from the injection nozzle and starts to rise, particles migrate faster from the sides to the channel center in the wake of the bubble. This leads faster to a higher flow resistance to fluid flow that translates into a higher pressure drop across the bed. This overall faster dynamics results in a larger amplitude of pressure drop oscillations for low μ_C as illustrated in Figure 20.

For high values of μ_C, particles displacement is more hindered due to higher friction with surrounding particles. Consequently, fluid bubbles are thinner, generally no more than the nozzle width. Particles are carried to the bed surface with a lower velocity as energy is dissipated by particle−particle tangential friction. Particles are also propelled with a lower velocity. The resulting bed height is then smaller as presented in Figure 19d. Particles settle laterally closer to the channel. It is rather visible that the time-averaged free surface of the bed (from the channel to the walls) has a remarkable upward oriented conic shape for high μ_C, while for low μ_C the cone is downward oriented. As a new bubble detaches from the injection nozzle and starts to rise, particles migrate rather slowly from the sides to the channel center in the wake of the bubble, such that resistance to fluid flow is almost continuous. As a result, the pressure drop across the bed does not fluctuate much over time as shown in Figure 20. The influence of μ_C on the pressure drop across the bed is summarized in Figure 21. It is rather obvious that the lower the friction coefficient is, the more frequent and the larger the pressure oscillations are.

6. CONCLUSION AND PERSPECTIVES

We presented a two-way Euler/Lagrange (DEM-CFD) numerical model for the simulation of fluid/solid flows. The mass and momentum conservation equations are discretized by a second order in space Finite Volume/Staggered Grid scheme. The Lagrangian tracking of particles with collisions is carried out with a Discrete Element Method. The coupled system of equations is advanced in time by a first-order operator-splitting algorithm. Finally, the fluid−solid momentum transfer is modeled at the discrete level by a simple but conservative projection operator. Our projection operator, also referred to in the literature as averaging operator or filter, is grid size dependent. Although very robust as it smoothes out time-dependent terms in a reliable way, it does not enable to refine the grid below the particle diameter.

We carefully evaluated the sensitivity of our numerical model to the following numerical parameters: solid time-step magnitude, fluid time-step magnitude, and grid size. The objective is to better control the quality of the computed solution based on detailed bed statistics. In the case of bubbling fluidized beds, we derived guidelines to produce results of reliable accuracy

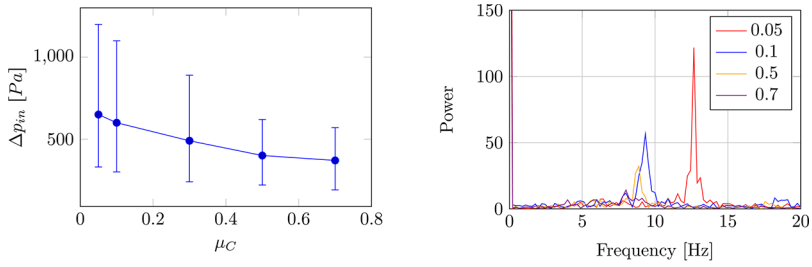

(a) Average, minimum and maximum pressure drop (b) Power spectrum

Figure 21. Influence of the Coulomb friction coefficient on the pressure drop across the bed in the single-nozzle spouted bed.

DOI: 10.1021/acs.iecr.6b03627

both in space and time that can be easily extrapolated. We also assessed the parallel computing performance of our numerical implementation. The preliminary tests carried out exhibit a very satisfactory scalability. In systems in which dynamic load balancing is not necessary, i.e., the number of particles per subdomain (core) does not vary much over time, as bubbling fluidized beds, computations with up to a hundred millions of particles on a few hundreds of core can be performed as a standard computation with our code. The extension to a few hundreds of millions on a few thousands of cores seem reasonably attainable too.

In a way to provide guidelines for more reliable benchmarks for fluidized bed simulations without lateral solid wall effects with DEM-CFD numerical models, we investigated the influence of the cross-section size of the biperiodic domain on the bed behavior. We showed than even in a biperiodic domain, selecting a certain cross-section size imposes flow structures that are not representative of the equivalent infinitely large fluidized bed the biperiodic computational domain is supposed to mimic. As the characteristic size of the flow structures is not easy to predict analytically or empirically, selecting the right domain cross-section size to yield computed results independent of the domain cross-section size has to be determined by numerical experiments. We illustrated this on a bubbling fluidized bed. In the flow regime investigated, the domain cross-section size needs to be roughly twice larger than the initial bed height and of the order of three-four times the size of the largest fluid bubble.

Our model was eventually validated against well documented experimental data relevant of a spouted bed with different injection configurations and different particle diameters. On this particular test case, our model performs quite well and agrees very satisfactorily with experimental data. Although this first validation step is promising, additional comparisons on more detailed flow markers are necessary. This is not necessarily straightforward as experimental measurements of these flow markers in the core of the bed as, e.g., particles velocity fluctuations, are still very challenging and experimental uncertainties can be quite large depending on the measurement technique employed.[46]

Finally, we investigated the influence of the Coulomb friction coefficient μ_C on the dynamics of a single-nozzle spouted bed. We showed that as tangential frictional resistance is increased by increasing μ_C, the overall bed dynamics is strongly affected. To summarize, low μ_C result in large and fast rising bubbles, particles propelled much higher than the average bed height and significant fluctuations of the pressure drop across the bed while high μ_C produce the reverse. This has important implications for industrial practices. In fact, over long operations, numerous high velocity collisions undergone by particles wear down (degrade) their surface, i.e., increase surface roughness, a phenomenon known as attrition. Since a spouted bed with smooth particles exhibit a markedly different dynamics than the same spouted bed with rough particles, this sheds some light on the fact that the corresponding industrial reactor might require to be operated differently over time to guarantee the same level of heat/mass transfer and thus a constant chemical conversion efficiency.

In terms of improvements of the numerical model, there are essentially two research paths to follow. The former concerns the use of a projection operator or filtering kernel independent of the grid size but instead dependent on the particle diameter. It is not only physically more sensible but also enables one to use any fluid grid size and hence potentially more accurately capture the fluid flow dynamics. In general, we expect any projection operator that conceptually decouples fluid grid size from particle size, e.g., offset method,[19] porous cube method,[36,37] or Gaussian filtering method,[6] to perform better than the embedding cube method suggested in this work. We recently implemented the Gaussian filtering method, and our simulation results confirmed that using this Gaussian filtering method further improves the quality of numerical results compared to using the embedding cube method. We intend to publish very soon this ongoing work in the scientific literature. The latter is the enhancement of the time algorithm to solve the coupled system of equations. In fact, our first-order operator splitting algoritm, although robust and efficient, is essentially a simple loose coupling algorithm. The development of strong coupling solution algorithms will undoutedly improve the time accuracy of the computed solutions.

AUTHOR INFORMATION

Corresponding Author

*E-mail: wachs@math.ubc.ca.

ORCID

Anthony Wachs: 0000-0002-8545-7688

Notes

The authors declare no competing financial interest.

REFERENCES

(1) Geldart, D. The effect of particle size and size distribution on the behaviour of gas-fluidised beds. *Powder Technol.* **1972**, *6*, 201−215.

(2) Geldart, D.; Cranfield, R. R. The gas fluidisation of large particles. *Chem. Eng. J.* **1972**, *3*, 211−231.

(3) Geldart, D. Types of gas fluidization. *Powder Technol.* **1973**, *7*, 285−292.

(4) Kidanemariam, A.; Uhlmann, M. Interface-resolved direct numerical simulation of the erosion of a sediment bed sheared by laminar channel flow. *Int. J. Multiphase Flow* **2014**, *67*, 174−188.

(5) Gidaspow, D. *Multiphase Flow and Fluidization: Continuum and Kinetic Theory Descriptions*; Academic Press, 1994.

(6) Pepiot, P.; Desjardins, O. Numerical analysis of the dynamics of two- and three-dimensional fluidized bed reactors using an Euler-Lagrange approach. *Powder Technol.* **2012**, *220*, 104−121.

(7) Tsuji, Y.; Kawaguchi, T.; Tanaka, T. Discrete particle simulation of two-dimensional fluidized bed. *Powder Technol.* **1993**, *77*, 79−87.

(8) Hoomans, B. P. B.; Kuipers, J. A. M.; Briels, W. J.; Van Swaaij, W. P. M. Discrete particle simulation of bubble and slug formation in a two-dimensional gas-fluidised bed: a hard-sphere approach. *Chem. Eng. Sci.* **1996**, *51*, 99−118.

(9) McNamara, S.; Young, W. R. Inelastic collapse and clumping in a one-dimensional granular medium. *Phys. Fluids A* **1992**, *4*, 496.

(10) Xu, B. H.; Yu, A. B. Numerical simulation of the gas-solid flow in a fluidized bed by combining discrete particle method with computational fluid dynamics. *Chem. Eng. Sci.* **1997**, *52*, 2785−2809.

(11) Hoomans, B. P. B. Comments on the paper "Numerical simulation of the gas-solid flow in a fluidized bed by combining discrete particle method with computational fluid dynamics" by B. H. Xu and A. B. Yu. *Chem. Eng. Sci.* **1998**, *53*, 2645−2646.

(12) Xu, B. H.; Yu, A. B. Authors reply to the comments of B.P.B. Hoomans, J.A.M. Kuipers, W.J. Briels and W.P.M. van Swaaij. *Chem. Eng. Sci.* **1998**, *53*, 2646−2647.

(13) Wen, C.; Yu, Y. H. Mechanics of fluidization. *Chem. Eng. Prog., Symp. Ser.* **1966**, *62*, 100.

(14) Ergun, S. Fluid flow through packed columns. *Chem. Eng. Prog.* **1952**, *48*, 89−94.

(15) Di Felice, R. Hydrodynamics of liquid fluidisation. *Chem. Eng. Sci.* **1995**, *50*, 1213−1245.

DOI: 10.1021/acs.iecr.6b03627

(16) Hill, R. J.; Koch, D. L.; Ladd, A. J. C. The first effects of fluid inertia on flows in ordered and random arrays of spheres. *J. Fluid Mech.* **2001**, *448*, 213−241.
(17) Hill, R. J.; Koch, D. L.; Ladd, A. J. C. Moderate-Reynolds-number flows in ordered and random arrays of spheres. *J. Fluid Mech.* **2001**, *448*, 243−278.
(18) Beetstra, R.; Van Der Hoef, M. A.; Kuipers, J. A. M. Drag force of intermediate Reynolds number flow past mono- and bidisperse arrays of spheres. *AIChE J.* **2007**, *53*, 489−501.
(19) Alobaid, F.; Ströhle, J.; Epple, B. Extended CFD/DEM model for the simulation of circulating fluidized bed. *Adv. Powder Technol.* **2013**, *24*, 403.
(20) Capecelatro, J.; Desjardins, O. An Euler-Lagrange strategy for simulating particle-laden flows. *J. Comput. Phys.* **2013**, *238*, 1.
(21) Feng, Y.; Yu, A. B. Comments on "Discrete particle-continuum fluid modelling of gas-solid fluidised beds" by Kafui *et al.* [Chem. Eng. Sci. 57 (2002) 2395−2410]. *Chem. Eng. Sci.* **2004**, *59*, 719−722.
(22) Kafui, K. D.; Thornton, C.; Adams, M. J. Discrete particle-continuum fluid modelling of gas-solid fluidised beds. *Chem. Eng. Sci.* **2002**, *57*, 2395−2410.
(23) Kafui, K. D.; Thornton, C.; Adams, M. J. Reply to Comments by Feng and Yu on "Discrete particle-continuum fluid modelling of gas-solid fluidised beds" by Kafui *et al. Chem. Eng. Sci.* **2004**, *59*, 723−725.
(24) Marchuk, G. I. Splitting and alternating direction methods. *Handb. Numer. Anal.* **1990**, *1*, 197−462.
(25) Marchuk, G. I.; Ruzicka, J. *Methods of Numerical Mathematics*; Springer-Verlag: New York, 1975; Vol. 2.
(26) Wachs, A.; Hammouti, A.; Vinay, G.; Rahmani, M. Accuracy of Finite Volume/Staggered Grid Distributed Lagrange Multiplier/Fictitious Domain simulations of particulate flows. *Comput. Fluids* **2015**, *115*, 154−172.
(27) Cundall, P. A.; Strack, O. D. L. A discrete numerical model for granular assemblies. *Geotechnique* **1979**, *29*, 47−65.
(28) Crowe, C. T.; Schwarzkopf, J. D.; Sommerfeld, M.; Tsuji, Y. *Multiphase Flows with Droplets and Particles*; CRC Press, 1997.
(29) Wachs, A.; Girolami, L.; Vinay, G.; Ferrer, G. Grains3D, a flexible DEM approach for particles of arbitrary convex shape-Part I: Numerical model and validations. *Powder Technol.* **2012**, *224*, 374.
(30) Wachs, A. A. DEM-DLM/FD method for direct numerical simulation of particulate flows: Sedimentation of polygonal isometric particles in a Newtonian fluid with collisions. *Comput. Fluids* **2009**, *38*, 1608−1628.
(31) Gilbert, E. G.; Johnson, D. W.; Keerthi, S. S. A fast procedure for computing the distance between complex objects in three-dimensional space. *Robotics and Automation, IEEE J.* **1988**, *4*, 193−203.
(32) Grest, G. S.; Dünweg, B.; Kremer, K. Vectorized link cell Fortran code for molecular dynamics simulations for a large number of particles. *Comput. Phys. Commun.* **1989**, *55*, 269−285.
(33) Schiller, L.; Naumann, Z. A drag coefficient correlation. *VDI Z* **1935**, *77* (1857−1968), 51.
(34) Huilin, L.; Gidaspow, D. Hydrodynamics of binary fluidization in a riser: CFD simulation using two granular temperatures. *Chem. Eng. Sci.* **2003**, *58*, 3777−3792.
(35) Benyahia, S.; Syamlal, M.; O'Brien, T. J. Extension of Hill-Koch-Ladd drag correlation over all ranges of Reynolds number and solids volume fraction. *Powder Technol.* **2006**, *162*, 166−174.
(36) Link, J. M. *Development and Validation of a Discrete Particle Model of a Spout-Fluid Bed Granulator*. Ph.D. Thesis, University of Twente,2006.
(37) Link, J. M.; Cuypers, L. A.; Deen, N. G.; Kuipers, J. A. M. Flow regimes in a spout-fluid bed: A combined experimental and simulation study. *Chem. Eng. Sci.* **2005**, *60*, 3425−3442.
(38) Wachs, A.; Vinay, G.; Hammouti, A. PeliGRIFF. http://www.peligriff.com.
(39) Feng, Y. Q.; Yu, A. B. Assessment of model formulations in the discrete particle simulation of gas-solid flow. *Ind. Eng. Chem. Res.* **2004**, *43*, 8378−8390.
(40) Ristow, G. H. Dynamics of granular materials in a rotating drum. *Europhys. Lett.* **1996**, *34*, 263.
(41) Thompson, P. A.; Grest, G. S. Granular flow: friction and the dilatancy transition. *Phys. Rev. Lett.* **1991**, *67*, 1751.
(42) Anderson, T. B.; Jackson, R. Fluid mechanical description of fluidized beds. Equations of motion. *Ind. Eng. Chem. Fundam.* **1967**, *6*, 527−539.
(43) Kunii, D.; Levenspiel, O. *Fluidization Engineering*; Butterworth-Heinemann: Boston, 1991; Vol. 2.
(44) Brown, S. L. *Hydrodynamics and Transient Heat Transfer Characteristics in Fluidized and Spouted Beds*. M.Sc. Thesis, Virginia Polytechnic Institute and State University, 2012.
(45) Deb, S.; Tafti, D. Investigation of flat bottomed spouted bed with multiple jets using DEM-CFD framework. *Powder Technol.* **2014**, *254*, 387−402.
(46) Tebianian, S.; Dubrawski, K.; Ellis, N.; Cocco, R. A.; Hays, R.; Reddy Karri, S.; Leadbeater, T.; Parker, D.; Chaouki, J.; Jafari, R.; Garcia-Trinanes, P.; Seville, J.; Grace, J. Investigation of particle velocity in FCC gas-fluidized beds based on different measurement techniques. *Chem. Eng. Sci.* **2015**, *127*, 310−322.

DOI: 10.1021/acs.iecr.6b03627